

Direct observation of hillslope scale StorAge Selection functions in an experimental hydrologic system: Geomorphologic structure and the preferential discharge of old water

Minseok Kim¹, Till Hannes Moritz Volkmann¹, Yadi Wang¹, Ciaran J Harman², and Peter A. Troch¹

¹University of Arizona

²Johns Hopkins University

November 22, 2022

Abstract

Spatially-integrated water transport dynamics at the hillslope scale have rarely been observed directly, and underlying physical mechanisms of those dynamics are poorly understood. We present time-variable transit time distributions (TTDs) and StorAge Selection (SAS) functions observed during a 28 days tracer experiment conducted at the Landscape Evolution Observatory (LEO), Biosphere 2, University of Arizona, AZ, USA. The observed form of the SAS functions is concave, meaning that older water in the hillslope was discharged more than younger water. The concavity is, in part, explained by the relative importance of advective and diffusive water dynamics and by the geomorphologic structure of the hillslopes. A simple numerical examination illustrates that, for straight plan shape hillslopes, the saturated zone SAS function is concave when hillslope Peclet (Pe) number is large. We also investigated the effect of hillslope planform geometry on the SAS function: The more convergent the plan shape is, the more concave the SAS function is. A numerical examination also indicates that the unsaturated zone SAS function is concave for straight and convergent hillslopes, when the soil thickness is constant. The concavity of those sub-component SAS functions signifies that the hillslope scale SAS function is concave for straight or convergent plan shape hillslopes when the hillslope Pe number is high.

1 **Direct observation of hillslope scale StorAge Selection**
2 **functions in an experimental hydrologic system:**
3 **Geomorphologic structure and the preferential**
4 **discharge of old water**

5 **Minseok Kim**¹, **Till H. M. Volkmann**^{1,2}, **Yadi Wang**^{1,3}, **Ciaran J. Harman**^{4,5},
6 **Peter A. Troch**^{1,6}

7 ¹Biosphere 2, University of Arizona, Tucson, AZ, USA

8 ²Applied Intelligence, Accenture, Kronberg im Taunus, Germany

9 ³Department of Environmental Science, University of Arizona, Tucson, AZ, USA

10 ⁴Department of Environmental Health and Engineering, Johns Hopkins University, Baltimore, MD, USA

11 ⁵Department of Earth and Planetary Sciences, Johns Hopkins University, Baltimore, MD, USA

12 ⁶Department of Hydrology and Atmospheric Sciences, University of Arizona, Tucson, AZ, USA

13 **Key Points:**

- 14 • We present the StorAge Selection (SAS) functions observed in a hillslope scale ex-
15 perimental system.
- 16 • The observed SAS functions are concave, meaning that waters flowing out are mainly
17 older stored waters.
- 18 • Advective water dynamics and the hillslope geomorphologic structure explain the
19 concavity.

Corresponding author: Minseok Kim, minseok.h.kim@gmail.com

Abstract

Spatially-integrated water transport dynamics at the hillslope scale have rarely been observed directly, and underlying physical mechanisms of those dynamics are poorly understood. We present time-variable transit time distributions (TTDs) and StorAge Selection (SAS) functions observed during a 28 days tracer experiment conducted at the Landscape Evolution Observatory (LEO), Biosphere 2, University of Arizona, AZ, USA. The observed form of the SAS functions is concave, meaning that older water in the hillslope was discharged more than younger water. The concavity is, in part, explained by the relative importance of advective and diffusive water dynamics and by the geomorphologic structure of the hillslopes. A simple numerical examination illustrates that, for straight plan shape hillslopes, the saturated zone SAS function is concave when hillslope Péclet (Pe) number is large. We also investigated the effect of hillslope planform geometry on the SAS function: The more convergent the plan shape is, the more concave the SAS function is. A numerical examination also indicates that the unsaturated zone SAS function is concave for straight and convergent hillslopes, when the soil thickness is constant. The concavity of those sub-component SAS functions signifies that the hillslope scale SAS function is concave for straight or convergent plan shape hillslopes when the hillslope Pe number is high.

1 Introduction

Field studies of hydrologic transport have been an active area of research during last decades. Numerous field sites have been studied (e.g., Sklash et al., 1986; Anderson et al., 1997; McDonnell et al., 1998; Graham et al., 2010; Gouet-Kaplan et al., 2012; Jackson et al., 2016), and those experimental studies have uncovered detailed process controls on the transport, greatly improving our process-based understanding. For example, Sklash et al. (1986) found that pre-event water generally contributes more to discharge than event water in Maimai M8 catchment, New Zealand. McDonnell et al. (1998) and Jackson et al. (2016) emphasized the importance of hydraulic conductivity variation and subsurface topographic complexity in transport dynamics. However, we still lack process-based understanding of system scale transport measures (e.g., transit time distributions) at scales useful for upscaling, such as the hillslope scale (e.g., Troch et al., 2013; Fan et al., 2019).

51 Looking at system scale dynamics using a spatially integrated signature has been
52 suggested as a way forward (e.g., Klemes, 1986; Sivapalan, 2003). Such signatures would
53 allow direct comparison of system scale dynamics across sites (Sivapalan, 2003). Also,
54 if we understand the dominant underlying physical mechanisms of spatially-integrated
55 signatures, the knowledge gained may be transferred across sites and spatial scales (e.g.,
56 Sivapalan, 2003; McDonnell et al., 2007). For example, hillslope scale understanding of
57 the dynamics can serve as a building block of large scale models such as catchment scale
58 models and Earth System Models (e.g., Troch et al., 2013; Fan et al., 2019).

59 Transit time distributions (TTDs) have been used widely as a spatially-integrated
60 signature of hydrologic transport dynamics (e.g., McGuire & McDonnell, 2010; Gabrielli
61 et al., 2018). The TTDs encapsulate spatially integrated hydrologic transport using the
62 differences in timings between the arrival of water particles (or parcels) into a system
63 and the discharge of those particles. However, recent research has shown that dealing
64 with TTDs in transport modeling and mechanistically explaining TTDs is not easy (e.g.,
65 Botter et al., 2011; van der Velde et al., 2012; Ali et al., 2014; Harman, 2015; Kim et al.,
66 2016). TTDs are time-variable under unsteady conditions (e.g., Niemi, 1977; Botter et
67 al., 2010). There are two types of time variability: “external” and “internal” (Kim et
68 al., 2016; Harman et al., 2016). External transport variability arises from fluctuations
69 in incoming and outgoing fluxes, while internal transport variability describes time-varying
70 flow paths in response to time-varying forcings (Heidbüchel et al., 2013; Kim et al., 2016).
71 The external transport variability complicates parameterizing TTDs, and examining how
72 system structures and flow paths are reflected in TTDs (Kim et al., 2016).

73 The recently developed StorAge Selection (SAS) function framework can alleviate
74 some of these difficulties. Unlike TTDs, the SAS function does not directly explain the
75 timing difference of inflow and outflow of water particles, but rather relates the system’s
76 internal age structure to water transit time (or age of water at the time of discharge) (Botter
77 et al., 2011; van der Velde et al., 2012; Harman, 2015). The SAS function does not need
78 to account for external transport variability, only internal variability (Kim et al., 2016;
79 Harman et al., 2016; Wilusz et al., 2017; Yang et al., 2018; Kaandorp et al., 2018). (Ex-
80 ternal transport variability is accounted for when the SAS function is combined with the
81 flux time series to calculate the time-variable TTD.) The separation suggests that re-
82 lating internal structure and processes to the SAS function would be easier compared
83 to the TTDs.

84 However, we currently lack direct observation of the SAS functions (and TTDs)
85 at the hillslope scale or at the catchment scale. So far, most studies have calibrated the
86 SAS functions to reproduce the observed tracer dataset (e.g., van der Velde et al., 2014;
87 Harman, 2015; Benettin et al., 2017; Wilusz et al., 2017; Kaandorp et al., 2018) or rely
88 on numerical models (e.g., Danesh-Yazdi et al., 2018; Wilusz et al., 2020). While the cal-
89 ibrated SAS functions reproduce the tracer data set, there is no guarantee how close that
90 function is to the actual SAS function (e.g., Harman, 2019). For example, the calibrated
91 form may vary depending on a priori determined functional form used in a calibration
92 procedure. This limits our ability to understand underlying physical mechanisms of the
93 SAS function.

94 There is a method of directly observing the SAS functions and TTDs called PERTH
95 (Periodic Tracer Hierarchy)(Harman & Kim, 2014). PERTH requires periodic steady state
96 hydrodynamics which is impossible to achieve in large scale real systems. However, the
97 Landscape Evolution Observatory (LEO) hillslopes, Biosphere 2, University of Arizona,
98 AZ, USA, provide a unique opportunity to apply the PERTH method at the hillslope
99 scale. The three LEO hillslopes are 330 m³ artificial hillslopes in a controlled environ-
100 ment, capable of creating periodic steady state conditions. We conducted a PERTH tracer
101 experiment for 28 days in the LEO hillslopes, yielding direct experimental observations
102 of the SAS functions and TTDs. Here we report the results of those experiments, and
103 use simple low-order process-based models to explain the form of the observed SAS func-
104 tions. The structure of this manuscript is as follows. Section 2 provides a theoretical back-
105 ground on TTD and SAS functions. Section 3 describes the experimental setup and how
106 the PERTH method was applied. In section 4, we report the experimental results, in-
107 cluding the observed TTDs and SAS functions. In section 5, we explain the observed form
108 of the SAS function based on physical processes. This discussion includes development
109 of a low-order process-based model and its application to mechanistically explain the ob-
110 served SAS functions.

111 **2 Theoretical Background**

112 We will briefly describe the essential theoretical background for the transit time
113 distributions (TTDs) and the StorAge Selection (SAS) functions. The TTD represents
114 hydrologic transport dynamics using the difference between the time a water particle (or
115 parcel) enters a system and the time that the particle leave the system. The timing dif-

116 ference is transit time T . Two types of TTDs have been introduced: the forward TTDs
 117 (fTTDs), which describe the distribution of transit times of water that enters at an in-
 118 jection time t_i , and the backward TTDs (bTTDs), which describe the transit time of wa-
 119 ter that discharges at a time t . The bTTDs \overleftarrow{p}_Q relate the influx concentration C_J of a
 120 conservative tracer to the outflux concentration C_Q of the tracer as (e.g., Niemi, 1977):

$$121 \quad C_Q(t) = \int_{-\infty}^t C_J(t_i) \overleftarrow{p}_Q(t - t_i, t) dt_i \quad (1)$$

122 Once the bTTDs are determined, system scale conservative solute export can be
 123 modeled at a scale of interest using the equation above. However, functional form of the
 124 bTTDs are, in general, complicated under unsteady conditions, making direct applica-
 125 tion of the above equation difficult (e.g., van der Velde et al., 2014; Harman, 2015; Ri-
 126 naldo et al., 2015).

127 The StorAge Selection (SAS) function framework provides a way to reduce these
 128 difficulties (e.g., Rinaldo et al., 2015). The framework introduces the age-ranked stor-
 129 age S_T (Harman, 2015), which is the volume of water storage younger than a given age.
 130 The rank SAS function Ω_Q is the bTTDs mapped onto the age-ranked storage, that is:
 131 $\Omega_Q(S_T(T, t), t) = \overleftarrow{P}_Q(T, t) = \int_0^T p_Q(\tau, t) d\tau$. This simple mapping makes the SAS func-
 132 tions independent of the external variability and makes its form much simpler than TTDs.
 133 Once the SAS functions $\Omega_Q(S_T, t)$ are determined, time-evolution of the age-ranked stor-
 134 age can be estimated using (Harman, 2015):

$$135 \quad \frac{\partial S_T(T, t)}{\partial t} = J(t) - Q(t) \Omega_Q(S_T(T, t)) - \frac{\partial S_T(T, t)}{\partial T} \quad (2)$$

136 The SAS function can then be converted to the bTTDs using the estimated age-
 137 ranked storage to model hydrologic transport using (1).

138 **3 Experimental Setup**

139 **3.1 Landscape Evolution Observatory hillslopes**

140 The tracer experiment was conducted at the Landscape Evolution Observatory (LEO)
 141 hillslopes. The three LEO hillslopes are intended to be identical artificial hillslopes lo-
 142 cated inside the glass enclosure of Biosphere 2, University of Arizona, AZ, USA (e.g., Hopp

143 et al., 2009; Huxman et al., 2009; Pangle et al., 2015). The three hillslopes will be re-
144 ferred to as LEO east, LEO center and LEO west slopes, respectively. Each 330 m^3 (30
145 m long, 11 m wide, and 1 m deep) hillslope has a convergent topography with an aver-
146 age slope of 10° (Pangle et al., 2015). Figure 1A shows a 3-D rendering of the structure.
147 More information on the LEO hillslopes can be found elsewhere (e.g., Pangle et al., 2015;
148 Volkmann et al., 2018), and we only provide a brief summary of the relevant informa-
149 tion.

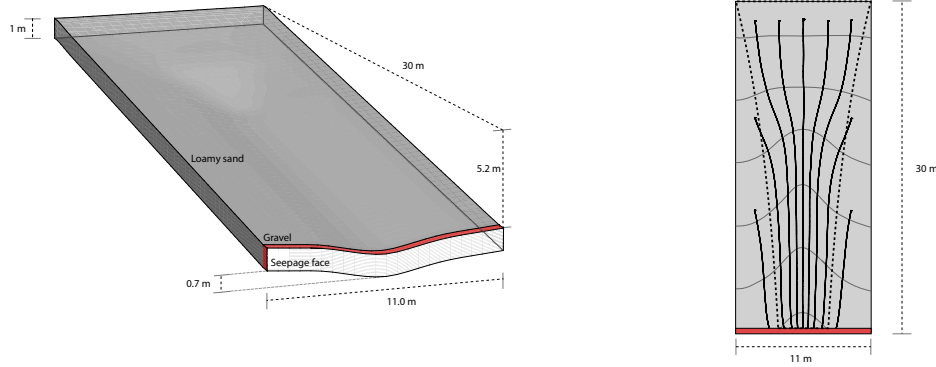
150 The steel structure is filled with basaltic tephra crushed to a loamy sand texture,
151 except the most downslope 5.5 m^3 (0.5 m long, 11 m wide, 1 m deep; see Figure 1A) where
152 a gravel-textured basaltic tephra is filled to facilitate lateral outflux. The average par-
153 ticle size fractions of the loamy sand textured crushed basaltic tephra are: 86.6% of sand
154 (50–2000 μm), 12.2% of silt (2–50 μm), and 3.2% of clay ($< 2 \mu\text{m}$) (Pangle et al., 2015).
155 The soil was packed layer by layer four times; 0.32 m thick wetted soil layers were added
156 and compacted to 0.25 m thick soil layer. A terrestrial laser scanner measured the soil
157 depth with 1 m resolution, and the measured depth is about 1 m (Pangle et al., 2015,
158 and see Figure 1B). The soil porosity is about 0.4 (Pangle et al., 2015). The saturated
159 soil hydraulic conductivity is about 10 m/day (which is the calibrated value in a previ-
160 ous modeling study of van den Heuvel et al. (2018)).

161 The LEO hillslopes provide a unique opportunity to conduct tracer experiments.
162 First of all, we can control the surrounding climate. A custom-engineered irrigation sys-
163 tem can supply water to the LEO landscapes with or without tracers. (The spatial ir-
164 rigation uniformity is achieved with the coefficient of variation of 0.2 at 13 mm/hr ir-
165 rigation intensity (Pangle et al., 2015).) Second, we can close the water mass balance
166 and the tracer mass balance with high precision and high time resolution. The lateral
167 outflow across the downslope boundary is divided into six sections, and the flow rate through
168 each section is measured every minute with a magnetic flow meter (SeaMetrics PE102;
169 1 % relative error at 0.11 – 11.4 L/min) and a tipping bucket (NovaLynx 26-2501-A).
170 Autosamplers (customized with a single channel peristaltic pump and an Adafruit In-
171 dustries stepper motor controlled by the Arduino Uno micro-controller board) collect seep-
172 age water samples at desired time intervals. An automated high-frequency (approximately
173 30 minutes) seepage water isotope analysis is also possible using an off-axis integrated-
174 cavity-output spectrometer (OA-ICOS, Log Gatos Research Inc.). The automated sys-
175 tem uses a four-channel peristaltic pump (Minipuls 3, Gilson Inc.) to deliver seepage wa-

(A) Hillslope structure

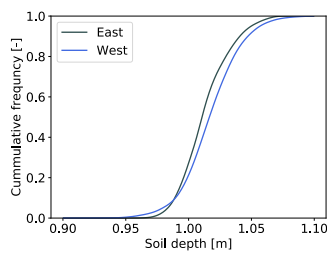
3-D view

2-D map



(B) Soil characteristics

Soil depth



Soil water retention curve and saturated porosity

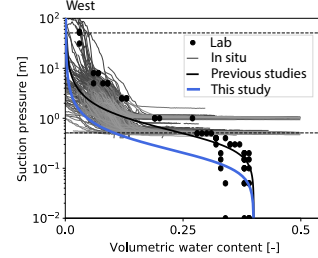
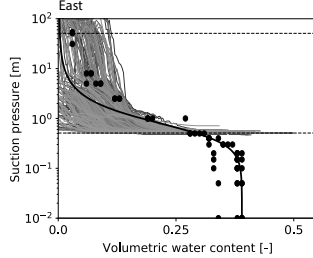


Figure 1. (A) Topological structure of the LEO hillslopes, and (B) Characteristics of the loamy sand textured soil. In the structure plots, the grey area represent loamy sand textured soil-filled area, and the red area represents the gravel-filled area. In the 2-D map, the thin solid lines are contours illustrating the elevation difference of 1 m, and the thick solid lines are hypothetical flow paths (along the steepest gradient of the steel structure). In the soil water retention curve plots, the grey lines are the in situ measurements, and the dots are the laboratory measurements. The black lines illustrate the van Genuchten curves that used in the previous numerical modeling studies of Niu et al. (2014) (for the east slope) and van den Heuvel et al. (2018) (for the west slope), and the blue line is the curve applied in this study. The dotted horizontal lines illustrate the working range of the MPS-2 sensor.

176 ter to a vaporization unit (Pangle et al., 2013). Thermo Scientific Dionex Ion Chromatog-
 177 raphy (DX-600), that analyze water chemistry, is also within reach. Furthermore, in or-
 178 der to track mass changes over time, 10 load cells (semi-custom Honeywell Model 3130)
 179 were installed under each hillslope structure.

180 The LEO hillslopes are also equipped with a dense internal sensor and sampling
 181 network. Soil water content is monitored at 496 locations in each hillslope using Decagon
 182 5TM every 15 minutes. The sensors were installed at five depths—154 sensors at 0.05
 183 m and 0.20 m depth, 76 sensors at 0.35 m depth, 78 sensors at 0.5 m depth, and 34 sen-
 184 sors at 0.85 m depth. 496 dielectric water potential sensors (Decagon MPS-2) are co-located
 185 with the soil water content sensors. Those sensors allow us to observe the in situ soil wa-
 186 ter retention curves (see Figure 1B). Pressure transducers (CS-451, Campbell Scientific,
 187 Inc.) were installed at 15 locations at the interface between the soil and the underlying
 188 steel structure. Assuming hydrostatic pressure, the measured pressure can be converted
 189 to water table height.

190 **3.2 Application of the PERTH method**

191 We adopted the PERiodic Tracer Hierarchy (PERTH) method (Harman & Kim,
 192 2014) to estimate the TTDs and the SAS functions of the LEO hillslopes. The PERTH
 193 method enables us to directly observe the time variable TTDs and the SAS functions
 194 with a small number conservative tracers (Harman & Kim, 2014; Kim et al., 2016; Pan-
 195 gles et al., 2017). The essential requirement for this method is a periodic steady state (PSS)
 196 with periodic inflow, storage and outflow time series. In this experiment, a simplified ver-
 197 sion of the method described in Harman and Kim (2014) was used, and we only describe
 198 the simplified method.

199 Let us denote with t_C the duration of each periodic cycle, with n_C the number of
 200 periodic cycles, and with N the number of irrigation events in each periodic cycle. Fol-
 201 lowing those notations, there are $n_C \times N$ irrigation events during the whole experimen-
 202 tal period. If each pulse in the first cycle was injected with a distinct conservative tracer,
 203 we observe N breakthrough curves (BTCs) $C_i(t)$ associated with the i th irrigation pulse,
 204 where $1 \leq i \leq N$ and i is an integer. (Note that, in this study, the BTC refers the
 205 concentration breakthrough curve normalized by its injection concentration and the back-
 206 ground concentration.) As the system is in the PSS, we can obtain the BTCs C_i asso-

207 ciated with the non-tracer labelled irrigation pulses $i \geq N$ by duplicating the observed
 208 BTCs as:

$$209 \quad C_i(t) = C_{(i \bmod N)}(t - \lfloor i/N \rfloor t_C) \quad (3)$$

210 for $N < i \leq n_C \times N$, and $C_0 = C_N$.

211 The backward transit time distribution $\overleftarrow{p}_Q(T, t)$ during the last cycle, i.e., $t \in [(n_C -$
 212 $1) \times t_C, n_C \times t_C]$ when the most information exists, can be estimated using C_i as (Harman
 213 & Kim, 2014):

$$214 \quad \overleftarrow{p}_Q(t - t_i, t) = \begin{cases} \frac{C_i(t)}{\Delta_i} & \text{if } J(t_i) > 0. \\ 0 & \text{otherwise.} \end{cases} \quad (4)$$

215 where Δ_i is the irrigation period of the pulse i . Note that, in the above equation,
 216 t_i determines the subscript i of C_i .

217 The age-ranked storage density s_T , which is the age-ranked storage differentiated
 218 with respect to age T ($s_T = \partial S_T / \partial T$), can be estimated using the bTTDs:

$$219 \quad s_T(t - \bar{t}_i, t) = \overline{J(t_i)} - \int_{t_i}^t Q(\tau) \overleftarrow{p}_Q(\tau - \bar{t}_i, \tau) d\tau \quad (5)$$

220 where \bar{J} is the averaged irrigation rate for each irrigation event.

221 The SAS function $\Omega_Q(S_T(T, t)) = \overleftarrow{P}_Q(T, t)$ can then be estimated using those func-
 222 tions, s_T and \overleftarrow{p}_Q . Note that, for this experiment, evaporation was not explicitly consid-
 223 ered, and the evaporated water was treated as if it had not entered the system. With
 224 the relatively low evaporated water volume (only about 9% or 6% of the irrigated wa-
 225 ter volume, see section 4 for details) and since young water sampling of evaporation is
 226 expected, its effect on the estimated SAS function is expected to be negligible.

227 We carefully designed the irrigation sequence to make as large fluctuations in stor-
 228 age and discharge as possible without generating overland flow. A storage-discharge re-
 229 lationship was used to design the irrigation sequence. The storage-discharge relationship
 230 was fitted to the dataset observed between June 1, 2016 to June 30, 2016 at the LEO

231 west hillslope. Based on the modeling, the sequence was determined as: $t_C = 3.5$ days
 232 with two 3 hours of 12 mm/hr irrigation events that are 7 hours apart (see Figure 2).

233 Deuterium (^2H), chloride (Cl), and bromide (Br) were selected as tracers. The Deu-
 234 terium labeled water was injected with the two irrigation pulses in the first cycle, and
 235 the Cl and Br labeled water was injected with each pulse in the cycle, respectively (see
 236 Figure 2). LiCl and LiBr were used to make the Cl and Br labeled water. In terms of
 237 the symbols used in (3), the normalized BTC of Cl is C_1 , and the normalized Br BTC
 238 is C_2 . The normalized deuterium BTC D was used to check the quality of C_1 and C_2
 239 using: $D = C_0 + C_1$. Injection tracer concentration of each tracer was determined sim-
 240 ilar to the previous tracer experiment conducted at the small version of the LEO hill-
 241 slope (Kim et al., 2016; Pangle et al., 2017). The determined injection concentration for
 242 each tracer is: $D^* = 500$ ‰, $C_0^* = 8000$ $\mu\text{mol/L}$, and $C_1^* = 8000$ $\mu\text{mol/L}$. The actual
 243 injection concentrations are: $D^* = 521$ ‰, $C_0^* = 7988$ $\mu\text{mol/L}$, and $C_1^* = 7992$ $\mu\text{mol/L}$.
 244 We collected seepage water every hour using the custom autosamplers for water chem-
 245 istry analysis. The real time isotope analysis system analyzed the deuterium enrichment
 246 of seepage water at approximately 30 minutes time interval for each slope.

247 4 Result

248 4.1 Water mass balance, periodicity, and break-through curves

249 The tracer experiment was conducted from December 1, 2016 to December 29, 2016.
 250 Figure 2A illustrates the time series of irrigation, discharge, storage, and the BTCs for
 251 the LEO east and the LEO west slopes. The irrigation system delivered nearly constant
 252 irrigation rate with some temporal fluctuations. We estimate the irrigation rate J based
 253 on the water mass balance using the observed discharge and the storage fluctuation; $J =$
 254 $Q + \Delta S / \Delta t$, where Q is the discharge rate, and $\Delta S / \Delta t$ is the storage fluctuation with
 255 $\Delta t = 1$ minute. Evaporation was assumed to be negligible during irrigation. Note that,
 256 in this paper, we do not present the results obtained at the LEO center hillslope. The
 257 center slope has a leak that accounts for about 15% of the mass-balance. The location
 258 of the leak is not yet identified, making it hard to explain the results mechanistically.

259 The storage S was estimated using its temporal fluctuation ($\Delta S / \Delta t$) that the load
 260 cells measured and the soil water content-based storage S_{swc} at time t_{swc} . While the SWC
 261 sensor data network is dense (496 sensors for each hillslope), the storage estimation us-

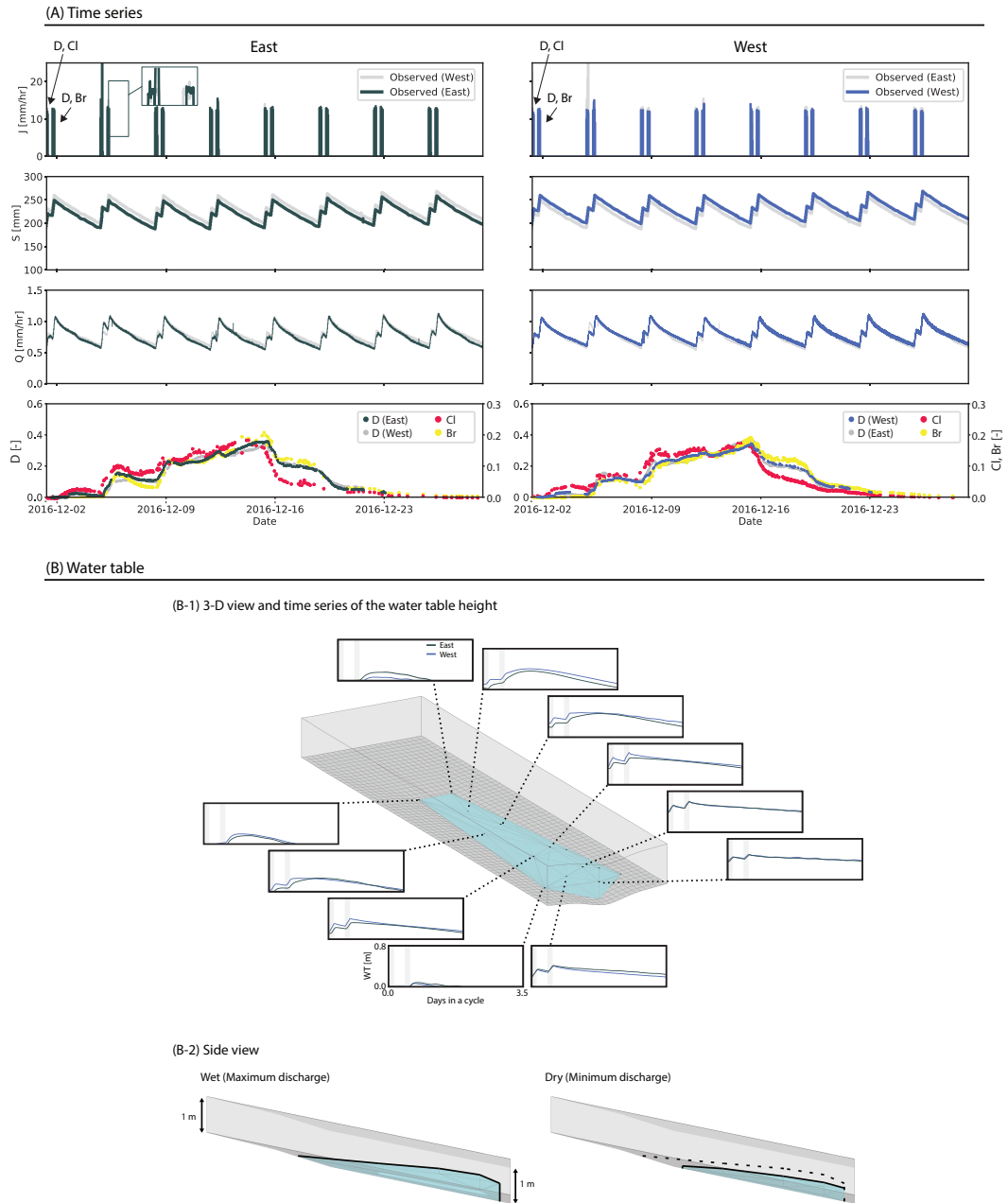


Figure 2. (A) Time series of the irrigation rate J , the total water storage S , the discharge rate Q , and the observed BTCs observed in the LEO east and the LEO west slopes. The grey lines illustrate the time series observed in the other hillslope for comparison. (B) Observed water table height and the saturated zone extent. (B1) Three-dimensional view of the LEO west hillslope saturated zone extent at the wet condition (at the maximum discharge) and the water table time series at each location in the both hillslopes. (B2) Side view of the observed water table at the wet condition and at the dry condition (at the minimum discharge). For visualization, the vertical scale is exaggerated by a factor of three. The dashed line in the side view of the dry condition figure shows the saturation zone extent at the wet condition, illustrating the water table fluctuation during the experiment.

262 ing the dataset required spatial interpolation and extrapolation. The nearest-neighbor
 263 method was used for both interpolation and extrapolation. t_{swc} was chosen as 8 am on
 264 January 23, 2017 when the hillslope averaged soil water content was about 0.1. The choice
 265 was to avoid overestimation since some in situ 5TM sensors overshoot at saturation (i.e.,
 266 recording values exceeding soil porosity) (Gevaert et al., 2014).

267 The mass balance-based total irrigation amount was 564 mm and 567 mm for the
 268 LEO east and the LEO west slope, respectively. The mean irrigation intensity was 11.7
 269 mm/hr and 11.8 mm/hr for those slopes. The total discharge amount during the exper-
 270 imental period was 513 mm and 532 mm, which give the runoff ratios of about 0.91 and
 271 0.94. We estimate the evaporation amount as an unaccounted component in the mass
 272 balance, 9% and 6% for the LEO east and the LEO west slopes, respectively. The to-
 273 tal evaporation amount was 50 mm and 34 mm, and the mean evaporation rate was 1.8
 274 mm/day and 1.2 mm/day, respectively. Pan evaporation rate measured at the toe of those
 275 hillslopes was about 2.4 mm/day, which is higher than the estimated mean evaporation
 276 rates.

277 Overall, the PSS was generated reasonably well except for the second cycle in the
 278 east hillslope. During the last hour of the second pulse in the cycle, the irrigation rate
 279 was doubled due to a malfunction of the irrigation system (see the top-left panel in Fig-
 280 ure 2). Thus, we did not irrigate water during the first hour of the following irrigation
 281 pulse, and the hillslope returned back to the PSS quickly. We examined the quality of
 282 the PSS by analyzing several observed time series using the same method that was used
 283 in Kim et al. (2016). The time series of irrigation, storage, and discharge were decom-
 284 posed into three components: trend (T), periodic (P), and random (R) components. The
 285 trend component is a 3.5 days moving average of the time series. The periodic compo-
 286 nent is an average of de-trended time series over each cycle, and the random component
 287 is the remaining signal. Because of the reason described above, the second cycle of the
 288 east hillslope was excluded from this analysis. A measure similar to the signal-noise ra-
 289 tio, $(Var(T) + Var(R))/(Var(P) + Var(T) + Var(R))$ was used to evaluate the rela-
 290 tive contributions of the aperiodic components to the total signal. These were 0.3% and
 291 0.9% for the irrigation rate, 4.0% and 2.3% for the storage, and 1.8% and 2.4% for the
 292 discharge rate, respectively. These low values indicate that the trend and random part
 293 are negligible compared to the periodic part. The trend component showed that stor-

294 age and discharge were increased almost linearly about 10 mm and 0.03 mm/hr, respec-
295 tively, throughout the experimental period, which were not significant.

296 The storage variation during each cycle was 60 mm around the average values of
297 223 mm and 230 mm for the east and west slopes, respectively. The extent of the sat-
298 urated zone also changed over time. Figure 2B illustrates the PSS-averaged water ta-
299 ble data estimated using data obtained from 15 pressure transducers by assuming hydro-
300 static pressure. The maximum water table fluctuation was 0.28 m and 0.27 m, respec-
301 tively, at the 13 m and 7 m upslope from the seepage face. Figure 2B-1 and 2B-2 illus-
302 trate the reconstructed 3-dimensional saturated zone extent. For the 3-dimensional il-
303 lustrations, Delaunay triangulation (Delaunay, 1934) was generated at each time step
304 using a set of 3-dimensional points of the observed water table. Since no extrapolation
305 was performed, the extent may be smaller than the actual saturated zone.

306 The tracer breakthrough curves (BTCs) are also illustrated in Figure 2. Thoses BTC
307 are normalized using the tracer injection concentrations and the background concentra-
308 tions. The BTCs observed at the two hillslopes are very similar. The mass recovery rates
309 for the deuterium tracer through discharge until December 23, 12 am, 2016 are 0.88 and
310 0.86 for the LEO east and the LEO west slopes, respectively. The mass recovery rates
311 for the Cl tracer until December 29, 8 am, 2016 are 0.87 and 0.90, and the rates for the
312 Br tracer are 0.93 and 0.94, respectively.

313 Looking at the time series of the irrigation, the discharge, and the tracer break-
314 through curves, the difference between velocity and celerity (e.g., Torres et al., 1998; Mc-
315 Donnell & Beven, 2014) at the hillslope scale is clear. During the entire experimental
316 period, the hydrologic cycle controlled by celerity was repeated 7 times. However, the
317 tracer BTCs started to increase after the first peak of the discharge and generally increased
318 to those peaks observed in the 5th cycle. That means that the pressure wave that con-
319 trols the hydrologic cycle was transmitted through the system at a much faster rate than
320 the actual velocity that controls the propagation of tracer-labeled water. The Cl and Br
321 BTCs are similar to the D BTC but show a little different dynamics in terms of timing.
322 The Cl tracer BTC is the fastest among other tracer BTCs since the Cl tracer was only
323 introduced with the first irrigation pulse. The Br BTC is the slowest, and the D BTC
324 is in the middle.

4.2 Transit time distributions and the StorAge Selection functions

The backward TTDs and the SAS functions can be estimated using the observed BTCs and using (4) and (5). Figure 3 illustrates the estimated cumulative bTTDs and the cumulative SAS functions. The bTTDs in those hillslopes are very similar. The median transit time of the backward transit time is 11-15 days, which is comparable to the turnover time of about 11-12 days. The distributions are broadly sigmoidal, but with a staircase structure. This arises from the fact that discharged water must have arrived during irrigation periods. No water may have an age corresponding to a time in the past when the input rate J was zero. This structure is the result of external transport variability what makes TTDs difficult to parameterize and explain mechanistically in time-variable flow systems.

As described earlier, the SAS functions do not reflect the external variability directly. Indeed, the observed SAS functions in these hillslopes are much smoother than the TTDs (see Figure 3B) and reveal some features of system scale transport more directly. The observed cumulative SAS functions is concave over most of the age-ranked storage, meaning that more older water is sampled for discharge than younger.

5 Discussion

The most notable feature of the observed SAS functions is the concave shape, which indicates that older water in the hillslope is more preferentially discharged. It is not immediately clear what contributes to the observed concavity. Only few tools (or models) link the functional form of the SAS function and TTDs directly to the hillslope geomorphologic and hydraulic properties and physical process (e.g., Gelhar & Wilson, 1974; Małoszewski & Zuber, 1982; Haitjema, 1995; van der Velde et al., 2012; Ameli et al., 2016; Kim, 2018). Most of those models predict linear or convex SAS functions. In other words, they suggest hillslopes release more younger water as discharge, or release all ages in proportion to their availability in storage.

For example, Gelhar and Wilson (1974) and Haitjema (1995) showed that 2-D idealized Boussinesq-type homogeneous aquifers with non-sloping impermeable layer and nearly-horizontal recharge boundaries have an exponential TTD in the saturated zone at steady state, which corresponds with a linear (or uniform) SAS function. If one further assumes that water particles injected over the hillslope soil surface spend more or

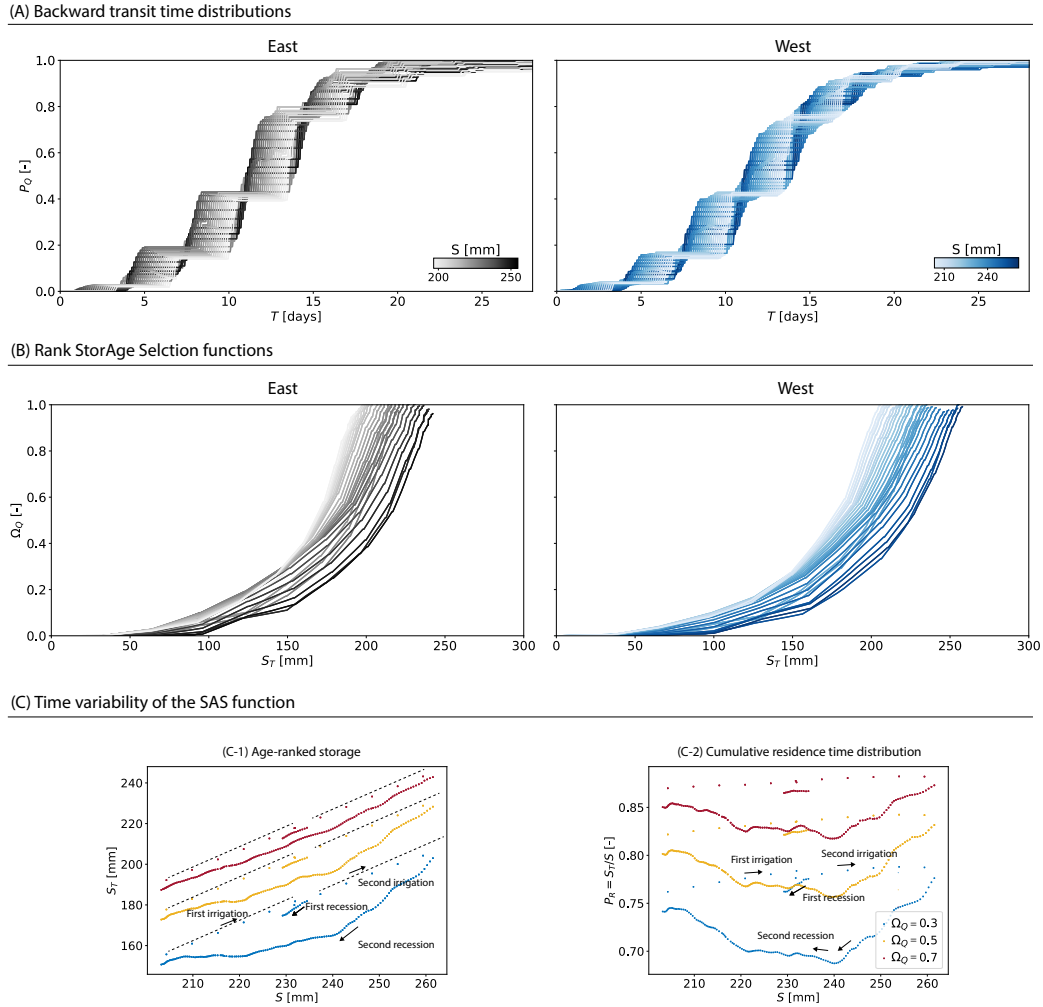


Figure 3. (A) Observed backward TTDs, (B) Observed SAS functions, and (C) LEO west SAS function time variability depending on total water storage. The bTTDs and SAS functions were plotted for every hour. Saturation of color indicates storage state from dry to wet. Panel (C) illustrates the age-ranked storage and the cumulative residence time distribution corresponding to three SAS function values: 0.3 (blue), 0.5 (yellow), and 0.7 (red). In (C-1), the dotted lines are the lines with the unit slope, approximating the observed dynamics during the irrigation periods.

356 less the same time in the unsaturated zone before those enter the saturated zone, one
357 can get piston-exponential distribution as a hillslope scale TTD (Małozewski & Zuber,
358 1982), which corresponds to a shifted linear SAS function. Kim (2018) showed that the
359 linearity is due to the approximately second-order polynomial water table profile esti-
360 mated by the Boussinesq equation, and in this case, the internal age structure does not
361 vary across lateral direction (characterized as “lateral symmetry”), resulting in a linear
362 SAS function. When the water table profile gradient gets higher downslope (and can-
363 not be approximate by a second-order polynomial), the 2-D Boussinesq aquifer discharge
364 is composed of more younger water, resulting in a convex-linear SAS function. The con-
365 vexity is pronounced for younger age-ranked storage while the SAS function is linear over
366 older water (Kim, 2018).

367 Some other models consider heterogeneous saturated hydraulic conductive struc-
368 tures. For example, Ameli et al. (2016) and Kim (2018) considered a decreasing satu-
369 ration hydraulic conductivity with depth, while Danesh-Yazdi et al. (2018) considered
370 stochastic hydraulic conductivity fields. These models predict linear or convex SAS func-
371 tions, and convex SAS functions indicate that more younger water contributes to dis-
372 charge compared to the model of Gelhar and Wilson (1974). In these models, the con-
373 tribution of more younger water is because the younger water moves laterally faster along
374 the shallower depth (because the hydraulic power is higher) or faster along the prefer-
375 ential flow path (determined by the stochastic hydraulic conductivity structure).

376 There is a notable exception where a model simulation predicts a concave SAS func-
377 tion. van der Velde et al. (2012) performed numerical modeling based on the Boussinesq
378 equation to estimate the saturated zone SAS function for several ideal hillslopes of $L =$
379 100 m, saturation hydraulic conductivity of 1 m/day, and downward slope depth of 1 m.
380 A hillslope with an inclined impermeable layer (slope of 4 %) results in the concave SAS
381 function when the steady recharge rate to the saturated area is 0.5 mm/day. The SAS
382 function of the hillslope becomes somewhat uniform as the recharge rate increases to 1.0
383 mm/day. As a result, it was concluded that when the sloping aquifer storage is low, it
384 samples more older water for discharge. However, because the result is specific to the
385 hillslope and the condition tested, it is not clear how van der Velde et al. (2012)’s result
386 explains the observed concavity in the LEO hillslope SAS functions. For example, it is
387 unclear how thick the hillslope saturated layer must be and how steep the impermeable
388 layer must be for the hillslope to drain more older water. In addition, van der Velde et

389 al. (2012) did not provide a process-based explanation of why the system drained more
 390 older water under those conditions. They did speculate that it might be related to the
 391 hillslope Péclet (Pe) number, a dimensionless number that explains the relative impor-
 392 tance of the advective water dynamics to the diffusive water dynamics (Berne et al., 2005).

393 Inspired by van der Velde et al. (2012)'s results, we test this hypothesis and check
 394 if the hillslope Pe number helps us to better describe the observed form of the SAS func-
 395 tion. The hillslope Pe number is a generalization of the hillslope number Hi (Brutsaert,
 396 1994) to take into account diverse hillslope plan shapes. If hillslope plan shapes can be
 397 approximated by an exponential function $ce^{-\alpha x/L}$, where x is the horizontal coordinate
 398 and $x = 0$ at the most upslope and $x = L$ at the most downslope, the hillslope Pe num-
 399 ber is given as: $Pe = \frac{L \tan a}{2pD} - \frac{\alpha}{2}$, where L is hillslope length, a is slope angle of the im-
 400 permeable layer, pD is the effective water table depth which can be estimated as a spa-
 401 tial average of water table height (Berne et al., 2005).

402 The hillslope Pe number for the LEO hillslopes was high during the experiment.
 403 A rough estimate of the hillslope Pe number is greater than 10 ($L \tan a = 5.2$ m, $2pD$
 404 less than 0.5 m and $\alpha \approx 1.0$). It's not clear how to estimate α since the hillslopes are
 405 convergent but not exponentially. Nevertheless, the exponentially converging hillslope
 406 with $\alpha = 1.0$ can approximate the major part of the LEO hillslopes (see Figure 1A).
 407 (Note that in this case, the uncertainty due to α is small when estimating the Pe num-
 408 ber.) The estimated high value means that the advective term in the Boussinesq equa-
 409 tion is important. This term was not considered in the model of Gelhar and Wilson (1974)
 410 that predicts a linear SAS function.

411 In what follows, we adopt most of the assumptions applied in the previous mod-
 412 els (e.g., Boussinesq-type aquifers and steady state) and investigate the effect of the slop-
 413 ing impervious layer and the hillslope plan shape on the hillslope scale SAS function. We
 414 also examine if the effects can be explained using the hillslope Pe number. The geomet-
 415 ric properties of the hillslopes we consider is: the hillslope length along the datum L , the
 416 exponential width function $ce^{-\alpha x/L}$, and the slope angle of the impermeable layer a . As
 417 mentioned earlier, the exponential width function may not be suitable for describing the
 418 geomorphologic structure of the LEO hillslopes. However, rather than focusing on the
 419 detailed topography of the LEO hillslopes, we choose the exponential function to pro-
 420 vide a more direct potential link to the previous hillslope scale theoretical studies where

421 the function was applied (e.g., Troch et al., 2002, 2003; Lyon & Troch, 2007; Norbiato
 422 & Borga, 2008). (Also note again that our purpose here is to investigate the origin of
 423 the concavity, not to provide a detailed model of the LEO hillslopes.)

424 We can use the framework developed by Kim (2018) to estimate the hillslope scale
 425 SAS function. They showed that if water particles that spend less time in the unsatu-
 426 rated zone also spend less time in the saturated zone, the hillslope scale SAS function
 427 can be constructed by a simple combination of the saturation zone SAS function and the
 428 unsaturated zone SAS function. Therefore, we first examine the saturated zone SAS func-
 429 tion and the unsaturated zone SAS function separately. These SAS functions are then
 430 combined to form the hillslope scale SAS function.

431 5.1 Saturated zone SAS function

432 We first determine the saturation zone using the Boussinesq equation. The hor-
 433 izontal velocity field used in the Boussinesq model is then used to determine the SAS
 434 function for the saturation zone. This section briefly describes the model and details are
 435 given in Appendix A. We first look at the effect of the impermeable layer slope, and then
 436 the effect of the hillslope plan shape. In the saturated zone model, we rotate the coor-
 437 dinate system if the impermeable layer slope $a > 0$, so that the x axis is parallel to the
 438 impermeable layer, and “horizontal” means parallel to the layer (see Figure 4A).

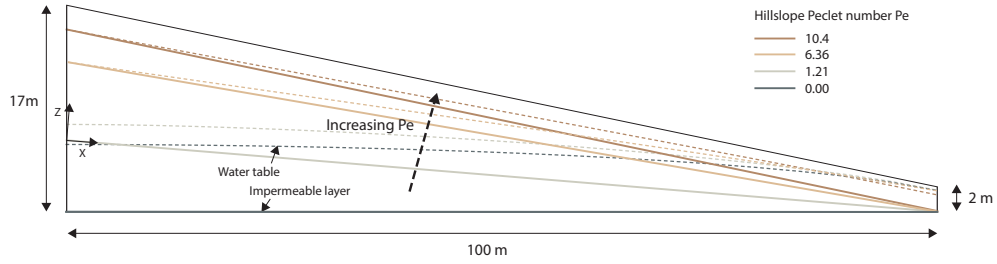
439 The Boussinesq model is based on the Dupuit-Forchheimer assumption, which can
 440 be interpreted that total hydraulic dissipation by vertical flow is negligible (e.g., Kirkham,
 441 1967; Haitjema, 2016). Under the assumption, vertical variation of lateral (horizontal)
 442 velocity is negligible. The assumption is generally applicable when the water level is rel-
 443 atively thin relative to its horizontal extent (Brutsaert, 1994). The model determines the
 444 water table, the water storage in the saturation zone, and the horizontal velocity field
 445 inside the saturation zone under steady-state. Using the lateral velocity field, we can es-
 446 timate the saturated zone transit time $T_s(x)$ of water particles recharged at x using (A4),
 447 and it also allows us to estimate the TTD using (A5). Once the TTD is estimated, the
 448 age-ranked storage can be determined using the SAS function framework’s governing equa-
 449 tion (2). We can then use the TTD and the age-ranked storage to estimate the SAS func-
 450 tion.

451 Using the model, a case study is firstly performed by estimating the SAS function
 452 for several cases with different hillslope Pe numbers. In this case study, the recharge rate,
 453 the saturated hydraulic conductivity, and the porosity are set to 5 mm/day, 2.5 m/day,
 454 and 0.4, respectively. The horizontal hillslope length L is set to 100 m. We set the slope
 455 of the impermeable layer to $a \in \{0.00, 0.05, 0.12, 0.15\}$ so that the Pe number varies.
 456 The boundary conditions are: no flow boundary condition at the upslope divide and the
 457 water table height $h = h_L$ at the downslope boundary. In the two high sloping cases,
 458 the downslope water table height boundary condition h_L is estimated using a kinematic-
 459 wave assumption-based model (e.g., Troch et al., 2002) which neglects the diffusive wa-
 460 ter dynamics; In other cases, it is set to 1.5 m, which is close to the kinematic-wave assumption-
 461 based model estimation for $a = 0.12$.

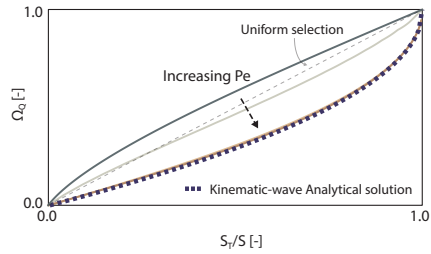
462 Figures 4A and B show the estimated water table profile, the hillslope Pe number,
 463 and the SAS function. The water level profile varies greatly depending on the hillslope
 464 Pe number. When the hillslope Pe number is zero, the water table is thicker at upslope.
 465 The total hydraulic head gradient is low at the upslope; thus water table builds up thicker
 466 at the upslope. As the hillslope Pe number increases, the thickest position moves downs-
 467 slope. When the hillslope Pe number is high enough ($Pe \geq 6.36$ in this case study), the
 468 water table forms the wedge-like shape, which is similar to the observed water table (see
 469 Figure 2B). In that case, the lateral gradient of total hydraulic head does not vary much
 470 across the hillslope (since the advective term dominates), and the water table is getting
 471 thicker downslope as more water pass through. The estimated SAS function shows that
 472 as the hillslope Pe number increases, the SAS function becomes more concave and even-
 473 tually converges to the analytical solution of the SAS function that is derived based on
 474 the kinematic-wave assumption (see Appendix B for its derivation).

475 In addition, 4000 simulations are performed by randomly selecting model param-
 476 eters. The sampling ranges are as follows: the recharge rate $J \in [1, 20]$ mm/day, $h_L \in$
 477 $[0.1, 2.95]$ m, $a \in [0.0, 0.2]$, porosity $n \in [0.2, 0.6]$, and the saturated hydraulic con-
 478 ductivity $k \in [0.5, 5.0]$ m/day. The results indicate that as the hillslope Pe number in-
 479 creases, the function converges to the concave analytical solution. When $Pe > 5$, the Kolmogorov-
 480 Smirnov (KS) distance (the maximum vertical distance between two cumulative distri-
 481 butions) between the SAS function and the kinematic-wave assumption-based SAS func-
 482 tion is less than 0.02 (see Figure 4C). The relationship between the KS distance and the
 483 hillslope Pe number is reduced to a single line, suggesting that the SAS function is pri-

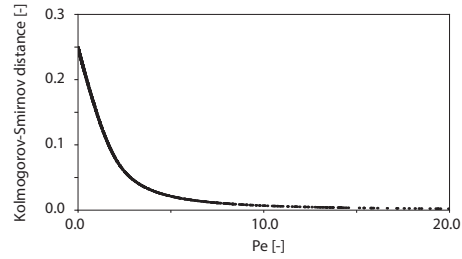
(A) Impermeable layer and water table



(B) SAS functions



(C) Smirnov-Kolmogorov distance



(D) Internal age structures [days]

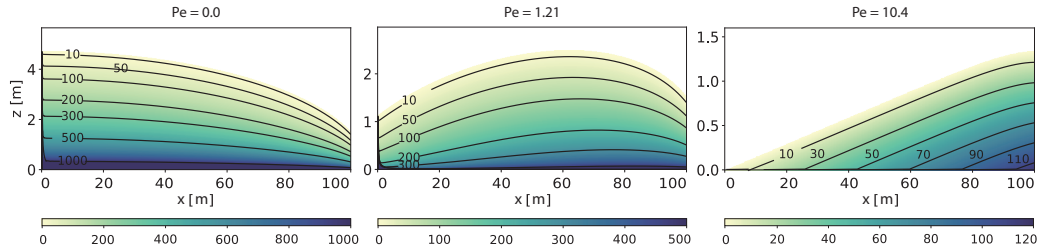


Figure 4. Water table profiles, SAS functions, and internal water age distributions for several hillslope Pe numbers. (A) Impermeable layer and water table profile, (B) SAS functions, (C) Kolmogorov-Smirnov distance between the kinematic-wave assumption-based analytical SAS function and the estimated SAS functions as a function of the hillslope Pe number, and (D) Internal water age distributions.

484 marily determined by the hillslope Pe number. In other words, the concavity of the SAS
485 function can be explained by the hillslope Pe number.

486 Spatial water age distributions help explain the trend. Figure 4D shows the dis-
487 tribution of water age in the saturation zone estimated based on mass-balance (see Ap-
488 pendix A for details on how to estimate the spatial age distribution). When Pe is zero,
489 the age structure is similar to the end-member case of “lateral symmetry” (Harman &
490 Kim, 2019). As mentioned earlier, the lateral symmetry exists when the height differ-
491 ence between the upslope water table and the downslope water table is small and the
492 water table profile can be approximated by a second order polynomial (Kim, 2018). The
493 SAS function associated with the end-member case “lateral symmetry” is a linear func-
494 tion (uniform or random sampling) since the age distribution of the discharge is the same
495 as the stored water age distribution. The age structure in the figure is a little different
496 from the end-member case especially at downslope locations where the hydraulic gra-
497 dient is steep. The estimated SAS function has convex form over the younger water stor-
498 age and has the linear form over the older water storage (see Figure 4C). The convex-
499 ity is related to the aforementioned steeper hydraulic head gradient at downslope loca-
500 tions; younger waters in discharge, which were injected at downslope locations, are con-
501 trolled by the steeper hydraulic head gradient at the downslope locations, yielding faster
502 lateral discharge (see Kim (2018) for more details).

503 In contrast, when Pe is high, old water is present only at the downslope part of the
504 hillslope (see Figure 4D). Unlike the low Pe cases, the old water recharged at upslope
505 went downhill due to the hydraulic head gradient similar to that of the impermeable layer
506 gradient (the advective component). Thus, old water present only at the downslope is
507 preferentially discharged, resulting in the concave SAS function. The age structure in
508 this high Pe case can be characterized by “water-table parallel”. Since the lateral flow
509 velocity does not change along the horizontal direction, the contours of the age distri-
510 bution move without deformation. Kim (2018) showed that the age structure is “water-
511 table parallel” when the saturated hydraulic conductivity declines with depth fast enough
512 so that the effect of impermeable layer on flow and transport is negligible. In that case,
513 advective water dynamics dominate the diffusion dynamics, which is similar to the high
514 Pe case.

515 However, the SAS functions in these cases are very different. In the case of decreasing
 516 hydraulic conductivity, young waters at shallower depth mobilizes faster, yielding the
 517 convex, younger water preference, SAS function (Kim, 2018). In the case of high Pe, the
 518 horizontal velocity does not change with the vertical direction, and due to the presence
 519 of a sloping impermeable layer, the old water only present around downslope, and it re-
 520 sults in a concave SAS function. This implies that the relative importance of the advective
 521 and diffusive water dynamics is important, but understanding which process deter-
 522 mines the relative importance (e.g., due to high Pe number or due to high Hi_X that was
 523 suggested in Kim (2018) for the declining hydraulic conductivity case) is more impor-
 524 tant in predicting the SAS function.

525 We also use the same model to examine the effect of the hillslope plan shape on
 526 the SAS function. For simplicity, we limit our interest to cases where the advective wa-
 527 ter dynamics dominate (i.e., when the kinematic-wave assumption holds). In this case,
 528 an analytic solution of the SAS function for the exponential width hillslopes can be de-
 529 rived, and the derivation steps are described in Appendix B. The analytical solutions show
 530 that the SAS function defined over the age-ranked storage normalized by the total stor-
 531 age (hence the fractional SAS function of van der Velde et al. (2012)) depends only on
 532 α . Figures 5A and 5B illustrate the hillslope plan shape and the associated SAS func-
 533 tions for several cases. The plan shapes are shown for the divergent ($\alpha = 3$), the straight
 534 ($\alpha = 0$), and the convergent ($\alpha = -3$) hillslopes, and the SAS functions are shown
 535 for $\alpha \in \{-3, -1, 0, 1, 3\}$. The results show that the more convergent the hillslope plan
 536 shape, the more concave the SAS function is (Figure 6B). As α increases, the SAS func-
 537 tion converges to the linear function. These results indicate that the concavity of the ob-
 538 served SAS functions may be due in part to the convergent geometry of the LEO hill-
 539 slopes.

540 The internal water age structures are all “water-table parallel” (see Figure 5C). There-
 541 fore, unlike the previous case, it is not easy to explain the difference in the SAS func-
 542 tions using the 2-D internal age structure. The more concave SAS function in the con-
 543 vergent hillslope is actually primarily caused by another dimension: width. In the con-
 544 vergent hillslope, the hillslope is wider at upslope where only younger water is present.
 545 This means that there is more younger water in the system that cannot be sampled by
 546 discharge compared to the straight hillslope and the divergent hillslope cases. It should
 547 also be noted that this trend does not coincide with the previous discussion on the hill-

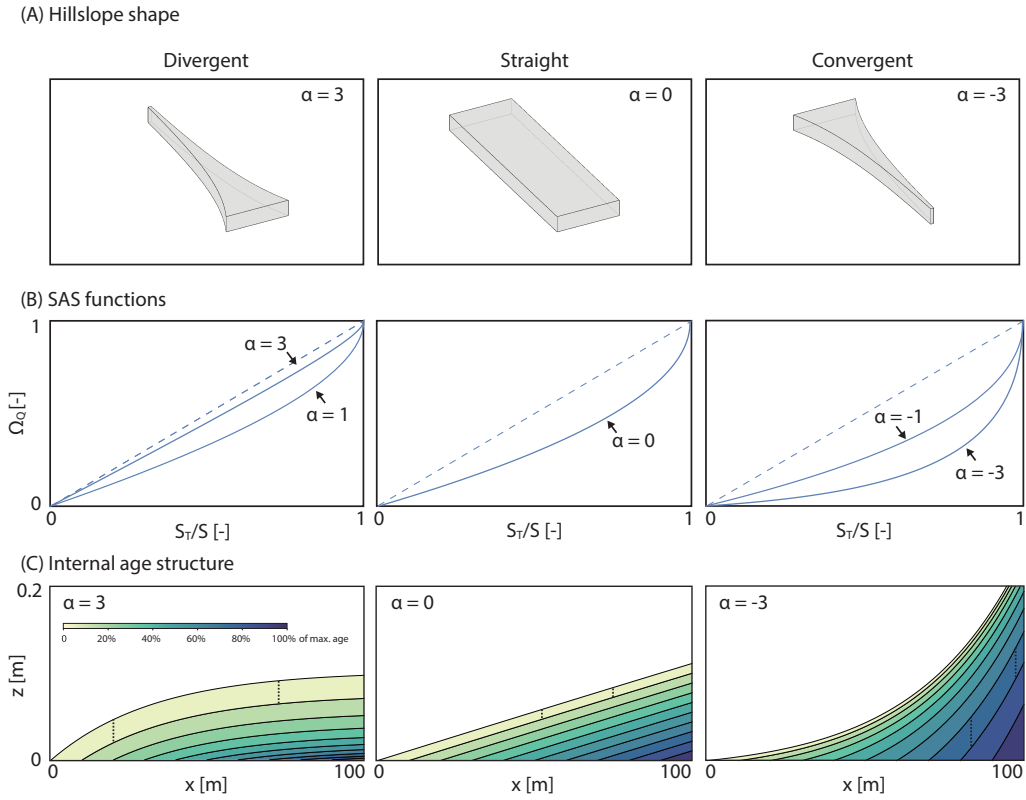


Figure 5. Hillslope plan shape, SAS function, and internal water age structure. (A) Hillslope plan shapes for $\alpha \in \{-3, 0, 3\}$. (B) Estimated SAS functions for $\alpha \in \{-3, -1, 0, 1, 3\}$. The dashed line illustrates the linear SAS function for comparison. (C) Internal water age structure. Each color represents 10% of the total age range. The two same length dotted lines in each figure indicate that the thickness of the same color region is constant, meaning that the age structure is “water-table parallel”.

548 slope Pe number for the straight hillslopes. The hillslope Pe number decreases for more
 549 convergent hillslopes, but the SAS functions become more concave. The SAS function
 550 becomes more convex for more divergent hillslopes which eventually converges to the lin-
 551 ear function. This is in contrast to the previously discussion for the straight hillslopes.
 552 Therefore, the hillslope Pe number alone is not sufficient for predicting the SAS func-
 553 tion. The plan shape must also be considered.

554 **5.2 Unsaturated zone SAS function**

555 In estimating the unsaturated zone SAS function, we assume that water moves mostly
 556 vertically, and the unsaturated zone dynamics can be modeled as a set of one-dimensional
 557 soil columns operating independently. With this assumption, the recharge rate to the
 558 saturated zone is equal to the (steady) irrigation rate. This means that the tension sat-
 559 urated zone where lateral flow can occur is included in the saturation zone in this model,
 560 and the lateral flow in the tension saturated zone is treated in the same way as estimat-
 561 ing the saturated zone lateral flow. This section briefly describes the model (see Appendix
 562 C for more information on the unsaturated zone model).

563 Since the LEO hillslopes are characterized with a high Pe number, we focus on the
 564 hillslope where the kinematic-wave assumption holds. It is also assumed that the soil thick-
 565 ness is constant, similar to the LEO hillslopes. From this section, we have set some pa-
 566 rameters similar to the experiment: The steady irrigation rate is $J = 19$ mm/day, $L =$
 567 30 m, and $a = 10^\circ$. We estimate the unsaturated zone SAS function for three plan shapes,
 568 $\alpha = -1$, $\alpha = 0$, and $\alpha = 1$, and examine the effect of the plan shape on the SAS func-
 569 tion.

570 Richard's equation can be used to estimate the one-dimensional saturation profile
 571 over the hillslope length $x \in [0, L]$ (see equation (C1)). To apply Richard's equation,
 572 we need to determine the soil-water retention curve and the relationship between suc-
 573 tion pressure and hydraulic conductivity. The van Genuchten model was used to describe
 574 the soil-water retention characteristic, which can be written as (van Genuchten, 1980):
 575 $\theta(\psi) = \theta_r + (\theta_s - \theta_r) (1 + |\psi/\psi_A|^n)^{-m}$ where θ is water content, θ_r is residual water
 576 content, θ_s is saturated water content, ψ is suction pressure head ($\psi < 0$), ψ_A is a pa-
 577 rameter sometimes referred to as the air-entry pressure, n is the parameter related to
 578 the pore-size distribution, and $m = 1 - 1/n$. Van Genuchten-Mualem relationship (van

579 Genuchten, 1980) was used to describe the suction pressure head-hydraulic conductiv-
 580 ity relationship: $k_r(\psi) = (1 + |\psi/\psi_A|^n)^{-m/2}(|\psi/\psi_A|^{-1+n}(1 + |\psi/\psi_A|^n)^{-m} - 1)^2$.

581 We use the parameters for those relationships determined in a previous numerical
 582 study of the LEO west hillslope, but modify one of them. van den Heuvel et al. (2018)
 583 applied a three-dimensional Richard's equation-based model to the LEO west hillslope
 584 and calibrated those parameters to reproduce the observed discharge and storage dataset.
 585 The calibrated parameters are: $\theta_s = 0.4$, $\theta_r = 0.01$, $\psi_A = 0.44$ m, and $n = 2.25$
 586 (van den Heuvel et al., 2018). Since we assume that all lateral flows occur in the satu-
 587 rated zone, we reduce the extent of the tension saturated zone by changing ψ_A to 0.18
 588 m. The modified soil-water retention curve is shown in Figure 1B with the calibrated
 589 curve in the previous study. The value was chosen so that the model's total water stor-
 590 age (including the saturated zone water storage) approximates the average total water
 591 storage of 228 mm observed in the LEO west slope. A numerical simulation of Kim (2018)
 592 showed that the lateral flow is negligible when $n = 2$ and $\psi_A = 0.2$ m, indicating that
 593 the lateral flow in the unsaturated zone in the model with the selected parameters is neg-
 594 ligible.

595 We estimate the soil moisture content profile $\theta_u(x_i, z)$, where $i \in [1, 100]$ and x_i
 596 is uniformly distributed over $[0, L]$, by discretizing the unsaturated zone into 100 soil columns
 597 and solving the one-dimensional Richard's equation. Then, the vertical downward ve-
 598 locity of water particles in the unsaturated zone can be estimated as: $J/\theta_u(x_i, z)$. The
 599 unsaturated zone transit time at x_i , $T_u(x_i)$, can be estimated by integrating the inverse
 600 of velocity over the column length, which is: $S_u(x_i)/J$ (see (C2)), where $S_u(x_i)$ is the
 601 water storage in the i th column. The transit time distribution is a histogram of $T_u(x_i)$
 602 (see (C3)), and the age-ranked storage and the SAS function can be estimated using the
 603 transit time distribution.

604 Figure 6A shows the estimated unsaturated zone SAS functions for the three cases
 605 ($\alpha = -1$, $\alpha = 0$, and $\alpha = 1$). The estimated SAS functions can be divided into two
 606 parts. The first part is where the SAS function is zero, and the second part is where the
 607 function is increasing. The first part exists because water must travel through some amount
 608 of unsaturated zone before it reaches the saturated zone, regardless of where the water
 609 is injected into the soil surface. Thus, the extent of the first part is related to the min-

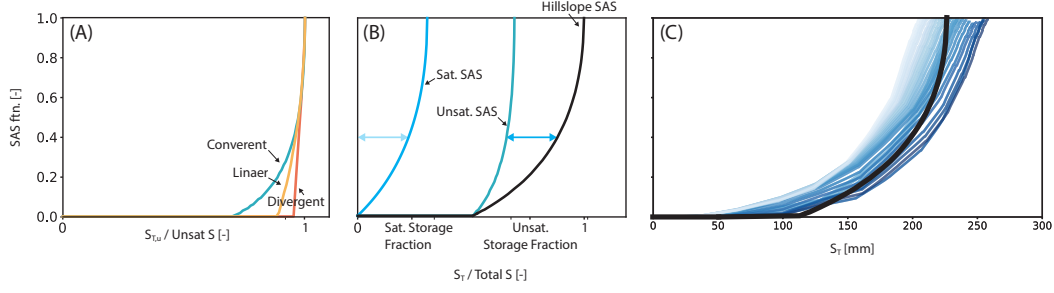


Figure 6. Sub component SAS functions and hillslope scale SAS functions. (A) Unsaturated zone SAS functions for $\alpha \in \{-1, 0, 1\}$. (B) Unsaturated zone, saturated zone, and hillslope scale SAS functions for $\alpha = -1$. The arrow lines are the same length lines, illustrating how the hillslope scale SAS function is estimated. (C) The observed SAS functions (the blue lines) and the estimated hillslope scale SAS function for $\alpha = -1$. The color saturation of the observed SAS functions illustrates the wetness condition from dry (light blue) to wet (dark blue).

imum value of $S_u(x_i)$. The extent is narrower for the convergent hillslope because water table builds up thicker in the convergent hillslope.

In the second part, the more convergent the hillslope, the more concave the SAS function. The shape of the SAS function in the unsaturated zone is largely determined by the plan shape and the water table profile. In the convergent hillslope, the SAS function becomes more concave as more water enters and exits at upslope with longer transit times. In addition, the water table profile is concave in the hillslope. Therefore, the water recharged into the saturated zone consists of a greater fraction of older water.

5.3 Hillslope scale SAS function

We can construct a hillslope scale SAS function using the saturated zone SAS function and the unsaturated zone SAS function, when both $T_u(x)$ and $T_s(x)$ decrease as x increases (Kim, 2018). The condition holds for the three cases considered in the previous section; $T_u(x)$ decreases with x since water table is thicker at downslope; $T_s(x)$ decreases with x since the flow pathway is getting shorter. When the condition is met, the hillslope scale SAS function $\Omega_Q(S_T)$ can be estimated using the inverse function of unsaturated zone SAS function $S_{T,u}(\Omega_Q)(= \Omega_Q^{-1}(S_{T,u}))$ and the inverse function of the saturated zone SAS function $S_{T,s}(\Omega_Q)(= \Omega_Q^{-1}(S_{T,s}))$ as: $\Omega_Q^{-1}(S_T) = S_T(\Omega_Q) = S_{T,u}(\Omega_Q) + S_{T,s}(\Omega_Q)$ (see Appendix D and Kim (2018) for more details).

628 Figure 6B illustrates the saturated zone SAS function, the unsaturated zone SAS
629 function, and the hillslope scale SAS function for the convergent hillslope with $\alpha = -1.0$.
630 According to the model described earlier, the hillslope scale SAS function can be esti-
631 mated by adding the unsaturated zone age-ranked storage and the saturated zone age-
632 ranked storage corresponding to each value of the SAS function (see Figure 6B). The es-
633 timated hillslope scale SAS function is concave, except for the flat zero probability in-
634 terval over the young age-ranked storage. The concavity of the hillslope scale SAS func-
635 tion is caused by the concavity of the sub component SAS functions, and the flat zero-
636 value area is determined by the unsaturated zone SAS function. Also, we can easily ex-
637 pect, for the linear planar hillslope, the hillslope scale SAS function to be concave with
638 a shift (the flat zero-value area). The function would converge to a shifted linear func-
639 tion when the planar shape is greatly divergent.

640 The similarity between the estimated hillslope scale SAS function and the observed
641 SAS function again suggests that the observed concavity could potentially be attributed
642 to the high hillslope Pe number and the convergent topography. The form of the esti-
643 mated hillslope scale SAS function for the convergent hillslope ($\alpha = 1.0$) is close to the
644 observed SAS function (see Figure 6C). Note again that the convergent planar shape (with
645 $\alpha = 1.0$) is different from the LEO hillslopes, but it still approximates the major part
646 of the LEO hillslopes (see Figure 1A).

647 This comparison between the observed SAS functions and the estimated SAS func-
648 tion shows a noteworthy difference. The observed SAS function increases earlier than
649 the modeled SAS function, which means that the model cannot capture very young wa-
650 ter in discharge. This may be because of the simplified unsaturated zone lateral flow and/or
651 preferential flow pathways. In the model, lateral flow occurs at the deepest possible depth.
652 So, if there is a smoother transition of lateral velocity along the vertical direction, the
653 hillslope can discharge more younger water at shallower depths than the model simulates.
654 In addition, while the soil in the hillslope is relatively homogeneous, there may still be
655 some preferential flow paths capable of draining younger water. More detailed exami-
656 nation using a 3-D Richards equation model is left for future study.

5.4 Broader implications: Hypothesizing dominant controls on the SAS functions

We have shown that the observed concavity is likely due to the advection-dominated dynamics, which is inferred from the high hillslope Pe number, and the convergent topography. The basic assumption that led to the conclusion is the relative homogeneity of the soil, which made it possible to apply the process-based model using effective parameters. The soil in the hillslopes were packed with an intention to make it homogeneous (Pangle et al., 2015). Also, given that 3-D Richard's equation-based model successfully reproduced a previous experiment using the effect parameters (van den Heuvel et al., 2018), the assumption seems to be valid in these hillslopes.

The process-based understanding based on the experimental observation may help to explain real-world SAS functions that were reported in previous studies. Some studies reported the convex (at wetter condition) - concave (at drier conditions) SAS functions (van der Velde et al., 2014; Rodriguez et al., 2018; Visser et al., 2019), while some other studies reported the convex SAS functions regardless of the wetness condition (Harman, 2015; Benettin et al., 2017; Wilusz et al., 2017; Kaandorp et al., 2018).

For studies that reported the convex-concave SAS functions, the studied sites are relatively steep (Gårdsjön G1, Sweden; Marshall Gulch, AZ, USA; H. J. Andrews WS10, Oregon, USA; Southern Sierra P301, California, USA) compared to other sites where the SAS functions are convex (Lower Hafren, Wales; Tanllwyth, Wales; Springendalse, Netherlands; Roelinksbeek, Netherlands; Bruntland Burn, Scotland). If we assume that the steepness of soil-bedrock interface (or a layer that supports lateral flow during the dry periods) is not very different from the steepness of the surface topography, it can be expected that the hillslope Pe number of those steep catchments would be high because saturated zone is thin under dry conditions. Therefore, the concavity of the SAS function in dry conditions may be due in part to the high hillslope Pe number. A similar conclusion was drawn in van der Velde et al. (2014) for the Marshall Gulch and the Gårdsjön G1 catchments, where they speculated that the concavity is due to the steep topography.

Under wet condition, there are several mechanisms that can contribute to sampling more fraction of young water, so making the SAS function more convex. For example, under wet conditions, the preferential flow may be dominant over the matrix flow (e.g., Lawes et al., 1882), which results in more heterogeneous flow pathways and more frac-

689 tion of younger water sampling (Berghuijs & Allen, 2019; Danesh-Yazdi et al., 2018). Also,
690 the G1 catchment is characterized with its steep exponential decline of the saturated hy-
691 draulic conductivity with depth (Nyberg, 1995). Thus, it is also possible that, under wet
692 conditions, faster lateral flow occurs at shallow depth where hydraulic conductivity is
693 high, resulting in more fraction of younger water sampling (e.g., Kim, 2018). Also, over-
694 land flow near a catchment outlet is another mechanism, among many others, that could
695 result in more younger water discharge under wet conditions.

696 The hypothesis, relating the concavity of the catchment scale SAS functions and
697 the high Pe number, is based on the limited number of studies. The hypothesis also has
698 the assumption that the process-based understanding gained under steady state can ac-
699 count for a certain characteristic of the SAS functions under unsteady state. Nonethe-
700 less, such process-based understanding on the form of the SAS functions help us develop
701 a hypothesis, which could be rejected with more thorough examinations at each site and
702 with further theoretical studies under unsteady state.

703 Some hypotheses for the convex SAS function in humid conditions are related to
704 soil evolution. The decrease in saturated hydraulic conductivity with depth or the pref-
705 erential flow path is more pronounced in mature soil. Those hypotheses for the convex
706 SAS function can be tested experimentally at the LEO hillslopes in future. The LEO
707 hillslopes were built to and have been operating to observe its evolution (e.g., Pangle et
708 al., 2015; Volkmann et al., 2018). We plan to introduce plants in the hillslopes that will
709 accelerate its evolution, and the LEO hillslopes will allow us to track how the SAS func-
710 tion evolves.

711 **5.5 On the time variability of the observed SAS functions**

712 In this paper, we mainly focused on explaining the general form of the observed
713 LEO hillslope SAS functions. Nevertheless, there are a few notable observations in terms
714 of time variability of these SAS functions. For example, the “inverse storage effect”, that
715 has been extensively inferred in catchment scale studies (e.g., van der Velde et al., 2014;
716 Harman, 2015; Wilusz et al., 2017; Benettin et al., 2017; Kaandorp et al., 2018), is not
717 observed in these hillslopes. The inverse storage effect is the widespread observation of
718 a larger fraction of younger water in discharge under wetter condition (Harman, 2015).
719 The observed LEO hillslope SAS functions during the irrigation periods shift primar-

720 ily to the right in response to irrigated additional water entering the unsaturated zone
 721 (see Figure 3B). This means that the LEO hillslopes preferentially discharge a larger frac-
 722 tion of older water under wet conditions, and so seem to behave somewhat differently
 723 than what has been observed at the catchment scale elsewhere.

724 Figure 3C-1 shows the time variability of the LEO west SAS function with stor-
 725 age S . As storage S increases, the age-ranked storage corresponding to several values
 726 of Ω_Q increases, suggesting the fractions they represent are getting older. During the ir-
 727 rigation periods, the corresponding age-ranked storage increases nearly by the amount
 728 of storage increment (see the black dotted lines). This figure also shows hysteresis. At
 729 the same total storage, younger stored water is preferentially discharged during the re-
 730 cession period than during the irrigation period. Physical processes that lead to the hys-
 731 teresis are not entirely clear and will be discussed in a subsequent numerical modeling
 732 study.

733 Figure 3C-2 is basically the same, but is plotted with the cumulative residence time
 734 distribution $P_R = S_T/S$ instead of the age-ranked storage S_T . The term “inverse stor-
 735 age effect” was originally introduced with the rank SAS function, that is defined over
 736 the age-ranked storage S_T , as a negative correlation between the rank SAS function scale
 737 parameter (of either a uniform or a gamma distribution) and storage. However, some-
 738 times this term has been used with the fractional SAS function that is defined over the
 739 cumulative residence time distribution rather than the age-ranked storage (e.g., Benet-
 740 tin et al., 2017; Kaandorp et al., 2018). Figure 3C-2 shows mostly the same character-
 741 istics as previously described based on Figure 3C-1, but with a noteworthy difference.
 742 During the later part of the second recession period, an inverse store effect-like behav-
 743 ior is observed. This indicates that one should be careful when investigating the inverse
 744 storage effect because its meaning could differ depending on which SAS function is used.
 745 Nevertheless, the general dynamics shown in this figure cannot be classified as the in-
 746 verse storage effect even in terms of the fractional SAS function, because the inverse stor-
 747 age effect is only present during a limited period.

748 It may seem that the LEO hillslopes are behaving differently than what has been
 749 observed in catchment scale studies, where the inverse storage effect is common. How-
 750 ever, recent studies on the origins of the inverse storage effect suggest the LEO behav-
 751 ior at the hillslope scale is not inconsistent with catchment scale inverse storage effects.

752 Several numerical modeling studies attribute the catchment scale inverse storage effect
753 to more diverse flow pathways or more complex soil hydraulic structure than might be
754 in the LEO hillslopes (e.g., Wilusz et al., 2020; Pangle et al., 2017). For example, Wilusz
755 et al. (2020) reported that their model simulated the inverse storage effect at the catch-
756 ment scale in Mahantango Creek experimental catchment, PA, USA. However, individ-
757 ual pathways in that catchment (e.g, direct runoff, overland flow, interflow, shallow ground-
758 water flow, and deep groundwater flow) did not show the inverse storage effect. They
759 concluded that the modeled catchment scale inverse storage effect is due to dispropor-
760 tional increase in contribution from each pathway to total discharge as the catchment
761 wets up. When the catchment is wet, it releases more water from pathways that deliver
762 younger water. In addition, Pangle et al. (2017) reported that the inverse storage effect
763 could be reproduced in a 2-D sloping aquifer block when saturation hydraulic conduc-
764 tivity decreases with depth. Such a hydraulic conductivity structure also increases the
765 contribution from water stored at shallower depths (which is younger) to discharge as
766 a hydrological system wets up.

767 **6 Conclusion**

768 We conducted a tracer experiment to observe the transit time distributions (TTDs)
769 and the StorAge Selection (SAS) functions in the Landscape Evolution Observatory (LEO)
770 hillslopes, Biosphere 2, University of Arizona, AZ, USA. The PERodic Tracer Hierar-
771 chy (PERTH) method was applied to observe those functions. The observed backward
772 TTDs are similar to Gaussian distribution with the median transit time of 11 - 15 days.
773 The observed SAS functions are concave, meaning that the hillslopes preferably discharged
774 older water in the system.

775 The observed form of the SAS functions is, in part, explained by the Hillslope Péclet
776 (Pe) number, which explains the relative controls of advective and diffusive water dy-
777 namics for homogeneous soil hillslopes. We show that, for linear planar hillslopes, as the
778 Pe increases, the saturated zone SAS function becomes concave and converges to the kine-
779 matic wave solution of the SAS function. We also examined the effect of the hillslope
780 planar shape on the SAS functions. A simple process-based model result shows that more
781 convergent hillslopes discharge more older water. Also, for the hillslope with a constant
782 soil thickness and characterized with high Pe number, the unsaturated zone SAS func-

783 tions show similar trend: The more convergent hillslope, the more concave SAS function.
 784 The concavity of those function results in the concave hillslope scale SAS function.

785 This process-based understanding help us hypothesize a process-based control on
 786 the calibrated SAS functions in other catchments. In most of the studies, the calibrated
 787 SAS functions are either convex (at wetter condition) - concave (at drier condition) or
 788 convex regardless of wetness conditions. We noticed that, for the catchment where the
 789 calibrated SAS functions are convex (wet) - concave (dry), topographic slope is higher
 790 than other catchments. It implies that the hillslope Pe number is high in those catch-
 791 ments at least under dry conditions, which might result in the concave SAS functions.
 792 At wetter condition, there might be other mechanisms, such as significant preferential
 793 flow, that result in the convex SAS function.

794 The LEO hillslopes will continue to provide exciting opportunities. Such prefer-
 795 ential flow pathways are more pronounced in mature soil, and the LEO hillslopes were
 796 built to and have been operating to observe its evolution. Currently, the LEO hillslopes
 797 are at the beginning, the bare soil stage. We plan to introduce plants which will accel-
 798 erate its evolution. Over time, the LEO hillslopes will show how the SAS functions evolve,
 799 and the result presented in this study could be used as a baseline.

800 **Appendix A The saturated zone transport model and the SAS func-** 801 **tions**

802 The model domain of interest has a sloping impermeable layer with the angle a ,
 803 and the saturated hydraulic conductivity is k and the soil porosity is n . We defined the
 804 2-D coordination system as (x, z) , where x is the axis parallel to the sloping imperme-
 805 able layer with $x = 0$ at the most upslope, and z is the axis orthogonal to the layer with
 806 $z = 0$ at the layer. The downslope boundary is at $x = L$.

807 Following the (extended) Dupuit-Forchheimer assumption, the Darcy flux $q_x(x)$
 808 in the saturated zone is (Childs, 1971):

$$q_x(x) = -k \left(\cos a \frac{\partial h}{\partial x} - \sin a \right) \quad (\text{A1})$$

809 where h is the total hydraulic head (and the water table height). The steady-state
 810 Boussinesq equation with a sloping impermeable layer, that solves water table height $h(x)$,
 811 can be written as (Childs, 1971):

$$0 = -\frac{d}{dx}(h(x)q_x(x)) + J' \quad (\text{A2})$$

812 where $J' = J \cos a$ is the recharge rate which is equivalent to the irrigation rate
 813 projected onto the rotated coordinate system. This second-order differential equation
 814 requires two boundary conditions which can be written as: $q_x(0) = 0$ and $h(L) = h_L$.

815 The horizontal (parallel to the impermeable layer hereafter) velocity in the above
 816 model can be written as:

$$v_x(x) = -\frac{k}{n}(\cos a \frac{dh(x)}{dx} - \sin a) \quad (\text{A3})$$

817 where n is porosity.

818 Using the horizontal velocity, we can formulate the transit time of a water parti-
 819 cle recharged at x_0 as:

$$T_s(x_0) = \int_{x_0}^L \frac{1}{v_x(x')} dx', \quad (\text{A4})$$

820 and the saturated zone TTD $P_{Q,s}$ is (Haitjema, 1995):

$$P_{Q,s}(T_s) = 1 - \frac{x_0(T_s)}{L} \quad (\text{A5})$$

821 The age-ranked storage $S_T(T)$ can be estimated using (2) and, under steady-state,
 822 it can be simplified as:

$$S_T(T) = J'(T - \int_0^T P_{Q,s}(T') dT') \quad (\text{A6})$$

823 Once the TTD $P_{Q,s}(T)$ and the age-ranked $S_T(T)$ are estimated, the SAS func-
 824 tion can be estimated by plotting $P_{Q,s}$ as a function of S_T .

825 Internal water age structure can also be estimated for the Boussinesq model. We
 826 track water particles using the above model by exploiting mass-balance. Let's say we la-
 827 bel a water particle that is recharged at x_0 . When it reaches $x = x_n (> x_0)$, the wa-
 828 ter recharged above its trajectory $J'(x_n - x_0)$ should flow laterally above its vertical lo-
 829 cation $z = z_n$; thus, $J'(x_n - x_0) = q_x(x_n)(h(x_n) - z_n)$. The vertical position z_n of the
 830 particle is:

$$z_n(x_n, x_0) = \frac{J'(x_0 - x_n)}{q_x(x_n)} + h(x_n) = \frac{J(x_n - x_0)}{k(h'(x_n) - \tan a)} + h(x_n) \quad (\text{A7})$$

831 The above equation can be inverted to estimate the injection location x_0 of a par-
 832 ticle at (x, z) as: $x_0(x_n, z_n) = x_n + k(h(x_n) - z)(h'(x_n) - \tan a)/J$. It allows us to es-
 833 timate the spatial age distribution $A(x, z)$ using:

$$A(x, z) = \int_{x_0(x, z)}^x \frac{1}{v_x(x')} dx' \quad (\text{A8})$$

834 **Appendix B Analytical solution of the saturated zone SAS functions** 835 **under the kinematic-wave assumption**

836 The saturated zone model can be simplified when the hillslope (Pe) number is suf-
 837 ficiently high (e.g., Beven, 1981; Brutsaert, 1994; Berne et al., 2005) since the diffusive
 838 water dynamic is negligible. We use the Hillslope-storage kinematic-wave model (Troch
 839 et al., 2002), which neglects the diffusive water dynamic and considers diverse hillslope
 840 plan shapes. The model assumes that transversal direction (i.e., orthogonal to both hor-
 841 izontal and vertical directions) gradient of total hydraulic head is negligible. With those
 842 simplifications, the lateral (horizontal) velocity (A3) becomes:

$$v_x = \frac{k}{n} \sin a, \quad (\text{B1})$$

843 and the transit time $T_s(x)$ for waters recharged at x_0 is:

$$T_s(x_0) = \frac{n(L - x_0)}{k \sin a} \quad (\text{B2})$$

844 When considering the plan shape, the model (A5), which determines the TTD, needs
 845 to be re-formulated. With the width function $w(x) = ce^{-\alpha x/L}$, the TTD $P_{Q,s}(T)$ can
 846 be formulated as:

$$P_{Q,s}(T_s) = 1 - \frac{1}{A} \int_0^{x_0(T_s)} w(x) dx = \frac{e^{\alpha \frac{T_s v_x}{L}} - 1}{e^\alpha - 1} \quad (\text{B3})$$

847 where A is the area of the hillslope.

848 Using the $P_{Q,s}(T_s)$ and (A6), the age-ranked storage can be estimated, and the SAS
 849 function can be written as:

$$\Omega_{Q,s}(S_{T,s}) = \frac{1 + e^\alpha W_p \left(-e^{-\alpha - \cosh \alpha + \sinh \alpha + \frac{\alpha e^{-\alpha} (e^\alpha - 1) v_x S_{T,s}}{J'L}} \right)}{1 - e^\alpha} \quad (\text{B4})$$

850 where $S_{T,s}$ is the saturated zone age-ranked storage, $W_p(x)$ is the Lambert-W func-
 851 tion with $p = \frac{\text{Sgn}(x)}{2}$, and $\text{Sgn}(x)$ is the sign function (Abramowitz & Stegun, 1974).
 852 The Lambert-W function is $W_p(ze^z) = z$ with $p = -1$ for $z < 0$ and $p = 0$ for $z \geq 0$
 853 (Corless et al., 1996).

854 When $\alpha \rightarrow 0$, so when the plan shape is straight, the SAS function becomes:

$$\Omega_{Q,s}(S_{T,s}) = 1 - \sqrt{1 - \frac{2k \tan a}{JLn} S_{T,s}} \quad (\text{B5})$$

855 In the form of the fractional SAS function $\Omega_{Q,s}^f$, which is defined over the cumu-
 856 lative residence time distribution $P_{R,s} = S_{T,s}/S_s$, where S_s is the saturated zone stor-
 857 age, those functions can be formulated as:

$$\Omega_{Q,s}^f(P_{R,s}) = \frac{1 + e^\alpha W_p \left(-e^{\alpha(P_{R,s}-1) + e^{-\alpha}(P_{R,s}-1) - P_{R,s}} \right)}{1 - e^\alpha}, \quad (\text{B6})$$

858 and when $\alpha \rightarrow 0$,

$$\Omega_{Q,s}^f(P_{R,s}) = 1 - \sqrt{1 - P_{R,s}}. \quad (\text{B7})$$

Appendix C The unsaturated zone transport model and the SAS functions

Let us denote 2-D water content field in the unsaturated zone as $\theta_u(x, z)$. If we assume that lateral flow in the unsaturated zone is negligible, the unsaturated zone water content $\theta_u(x, z)$ under the steady state can be estimated using the 1-D Richards equation:

$$0 = \frac{\partial}{\partial z} \left(k(\theta_u) \left(\frac{\partial \psi(x, z)}{\partial z} - 1 \right) \right) \quad (\text{C1})$$

where ψ is the matric head. In this study, we apply the steady flux rate J at the top soil $q = k(\frac{d\psi}{dz} - 1) = -J$ and the saturation condition at the bottom $\psi(h(x)) = 0$.

We can estimate the depth-integrated water storage in the unsaturated zone $S_u(x)$ as: $S_u(x) = \int_{h(x)}^{H(x)} \theta_u(x, z) dz$, where $H(x)$ is the soil thickness at x . Under steady state, the transit time $T_u(x)$ through the unsaturated zone can be estimated as:

$$T_u(x) = \int_{h(x)}^{H(x)} \frac{1}{v(x, z)} dz = \int_{h(x)}^{H(x)} \frac{1}{v(x, z)} dz = \frac{1}{J} \int_{h(x)}^{H(x)} \theta_u(x, z) dz = \frac{S_u(x)}{J} \quad (\text{C2})$$

where $H(\cdot)$ is the Heaviside (or unit) step function.

The transit time distribution can be formulated as:

$$P_{Q,u}(T) = \frac{1}{L} \int_0^L H(T - T_u(x)) dx = \frac{1}{L} \int_0^L H(JT - S_u(x)) dx \quad (\text{C3})$$

Using (A6), the age-ranked storage is:

$$S_{T,u}(T) = JT - \frac{1}{L} \int_0^L (JT - S_u(x)) H(JT - S_u(x)) dx = \frac{1}{L} \int_0^L \min(JT, S_u(x)) dx, \quad (\text{C4})$$

and the SAS function can be written as:

$$\Omega_{Q,u}(S_{T,u}) = \frac{1}{L} \int_0^L H(f^{-1}(S_{T,u}) - S_u(x)) dx \quad (\text{C5})$$

where $f(S_u(x)) = S_{T,u}$.

875 **Appendix D The hillslope scale SAS function**

876 We can construct the hillslope scale SAS function when there exists a monoton-
 877 ically increasing relationship between $T_u(x)$ and $T_s(x)$, let's say $T_s = q(T_u)$ where q is
 878 any monotonically increasing function. In that case, there exists a strictly increasing func-
 879 tion w that satisfies $T = T_u + T_s = w(T_u)$.

880 The hillslope scale TTD $P_Q(T)$ can be written as:

$$P_Q(T = w(T_u)) = P_{Q,u}(w(T_u)) = P_{Q,s}(T_s = q(T_u)), \quad (\text{D1})$$

881 and the age-ranked storage takes the form:

$$S_T(T) = S_{T,u}(w^{-1}(T)) + S_{T,s}(q(w^{-1}(T))) \quad (\text{D2})$$

882 The above equation implies that $S_T(\Omega_Q) = S_{T,u}(\Omega_Q) + S_{T,s}(\Omega_Q)$ and that the
 883 hillslope scale SAS function is the sum of the unsaturated zone SAS function and the
 884 saturated zone SAS function if we rotate the SAS function plot counter-clockwise 90 de-
 885 grees.

886 **Acknowledgments**

887 This work is supported by the National Science Foundation under grants EAR-1344552
 888 and EAR-1417175. The authors gratefully acknowledge support from the Philecology
 889 Foundation of Fort Worth Texas. Additional funding support was provided by the Of-
 890 fice of the Vice President of Research at the University of Arizona and by the Technol-
 891 ogy and Research Initiative Fund (TRIF) Water, Environmental, and Energy Solutions
 892 (WEES) initiative at the University of Arizona (Shared Equipment Enhancement Funds).
 893 Thanks to Aaron Bugaj, Nathan Abramson, Antonio Meira, Katarena Matos, John Adams,
 894 and Kimberly Land for their support during the experiment. The experimental dataset
 895 will be available at: <https://biosphere2.org>.

896 **References**

897 Abramowitz, M., & Stegun, I. A. (1974). *Handbook of Mathematical Functions*,

- 898 *With Formulas, Graphs, and Mathematical Tables*,. Dover Publications, Incorporated.
899
- 900 Ali, M., Fiori, A., & Russo, D. (2014, apr). A comparison of travel-time based catchment
901 transport models, with application to numerical experiments. *Journal of*
902 *Hydrology*, *511*, 605–618. doi: 10.1016/j.jhydrol.2014.02.010
- 903 Ameli, A., McDonnell, J. J., & Bishop, K. (2016). The exponential decline in saturated
904 hydraulic conductivity with depth: a novel method for exploring its
905 effect on water flow paths and transit time distribution. *Hydrological Processes*, *30*,
906 2438–2450. doi: 10.1002/hyp.10777
- 907 Anderson, S. P., Dietrich, W. E., Montgomery, D. R., Torres, R., Conrad, M. E., &
908 Loague, K. (1997). Subsurface flow paths in a steep, unchanneled catchment.
909 *Water Resources Research*, *33*(12), 2637–2653. doi: 10.1029/97WR02595
- 910 Benettin, P., Soulsby, C., Birkel, C., Tetzlaff, D., Botter, G., & Rinaldo, A. (2017).
911 Using SAS functions and high-resolution isotope data to unravel travel time
912 distributions in headwater catchments. *Water Resour. Res.*, *53*, 5375–5377.
913 doi: 10.1002/2013WR014979.Reply
- 914 Berghuijs, W. R., & Allen, S. T. (2019). Waters flowing out of systems are younger
915 than the waters stored in those same systems. *Hydrological Processes*. doi: 10
916 .1002/hyp.13569
- 917 Berne, A., Uijlenhoet, R., & Troch, P. A. (2005). Similarity analysis of subsurface
918 flow response of hillslopes with complex geometry. *Water Resources Research*,
919 *41*, 1–10. doi: 10.1029/2004WR003629
- 920 Beven, K. (1981). Kinematic subsurface stormflow. *Water Resources Research*,
921 *17*(5), 1419–1424. doi: 10.1029/WR017i005p01419
- 922 Botter, G., Bertuzzo, E., & Rinaldo, A. (2010, mar). Transport in the hydrologic
923 response: Travel time distributions, soil moisture dynamics, and
924 the old water paradox. *Water Resources Research*, *46*(3), 1–18. doi:
925 10.1029/2009WR008371
- 926 Botter, G., Bertuzzo, E., & Rinaldo, A. (2011, jun). Catchment residence and travel
927 time distributions: The master equation. *Geophysical Research Letters*, *38*(11),
928 L11403. doi: 10.1029/2011GL047666
- 929 Brutsaert, W. (1994). The unit response of groundwater outflow from a hillslope.
930 *Water Resources Research*, *30*(10), 2759–2763. doi: 10.1029/94WR01396

- 931 Childs, E. (1971). Drainage of groundwater resting on a sloping bed. *Water Re-*
 932 *sources Research*, 7(5), 1256–1263.
- 933 Corless, R. M., Gonnet, G. H., Hare, D. E. G., Jeffrey, D. J., & Knuth, D. E. (1996).
 934 On the Lambert W function. *Advances in Computational Mathematics*, 5(1),
 935 329–359. doi: 10.1007/BF02124750
- 936 Danesh-Yazdi, M., Klaus, J., Condon, L. E., & Maxwell, R. M. (2018). Bridg-
 937 ing the gap between numerical solutions of travel time distributions and
 938 analytical storage selection functions. *Hydrological Processes*, 32(8). doi:
 939 10.1002/hyp.11481
- 940 Delaunay, B. N. (1934). Sur la sphère vide. *Bulletin of Academy of Sciences of the*
 941 *USSR*(6), 793–800.
- 942 Fan, Y., Clark, M., Lawrence, D. M., Swenson, S., Band, L. E., Brantley, S. L.,
 943 ... Yamazaki, D. (2019). Hillslope Hydrology in Global Change Research
 944 and Earth System Modeling. *Water Resources Research*, 1737–1772. doi:
 945 10.1029/2018WR023903
- 946 Gabrielli, C. P., Morgenstern, U., Stewart, M. K., & McDonnell, J. J. (2018). Con-
 947 trasting Groundwater and Streamflow Ages at the Maimai Watershed. *Water*
 948 *Resources Research*, 54. doi: 10.1029/2017WR021825
- 949 Gelhar, L. W., & Wilson, J. L. (1974). Ground-Water Quality Modeling. *Ground*
 950 *Water*, 12(6), 399–408. doi: 10.1111/j.1745-6584.1974.tb03050.x
- 951 Gevaert, A. I., Teuling, A. J., Uijlenhoet, R., DeLong, S. B., Huxman, T. E., Pangle,
 952 L. A., ... Troch, P. A. (2014). Hillslope-scale experiment demonstrates the
 953 role of convergence during two-step saturation. *Hydrology and Earth System*
 954 *Sciences*, 18(9), 3681–3692. doi: 10.5194/hess-18-3681-2014
- 955 Gouet-Kaplan, M., Arye, G., & Berkowitz, B. (2012). Interplay between resident and
 956 infiltrating water: Estimates from transient water flow and solute transport.
 957 *Journal of Hydrology*, 458-459, 40–50. doi: 10.1016/j.jhydrol.2012.06.026
- 958 Graham, C. B., Woods, R. A., & McDonnell, J. J. (2010). Hillslope threshold re-
 959 sponse to rainfall: (1) A field based forensic approach. *Journal of Hydrology*,
 960 393(1-2), 65–76. doi: 10.1016/j.jhydrol.2009.12.015
- 961 Haitjema, H. (1995). On the residence time distribution in idealized groundwater-
 962 sheds. *Journal of Hydrology*, 172(1-4), 127–146. doi: 10.1016/0022-1694(95)
 963 02732-5

- 964 Haitjema, H. (2016). Horizontal Flow Models That Are Not. *Groundwater*, *54*(5),
 965 613. doi: 10.1111/gwat.12448
- 966 Harman, C. J. (2015). Time-variable transit time distributions and transport: The-
 967 ory and application to storage-dependent transport of chloride in a watershed.
 968 *Water resources research*, *51*, 1–30. doi: 10.1002/2014WR015707
- 969 Harman, C. J. (2019). Age-Ranked Storage-Discharge Relations: A Unified Descrip-
 970 tion of Spatially Lumped Flow and Water Age in Hydrologic Systems. *Water*
 971 *Resources Research*, *55*(8), 7143–7165. doi: 10.1029/2017wr022304
- 972 Harman, C. J., & Kim, M. (2014). An efficient tracer test for time-variable tran-
 973 sit time distributions in periodic hydrodynamic systems. *Geophysical Research*
 974 *Letters*, 1567–1575. doi: 10.1002/2013GL058980
- 975 Harman, C. J., & Kim, M. (2019). A low-dimensional model of bedrock weathering
 976 and lateral flow co-evolution: 1. Hydraulic theory of reactive transport. *Hydro-*
 977 *logical Processes*, *33*, 466–475. doi: 10.1002/hyp.13360
- 978 Harman, C. J., Ward, A. S., & Ball, A. (2016). How does reach-scale stream-
 979 hyporheic transport vary with discharge? Insights from rSAS analysis of se-
 980 quential tracer injections in a headwater mountain stream. *Water Resources*
 981 *Research*, *52*(9), 7130–7150. doi: 10.1002/2016WR018832
- 982 Heidbüchel, I., Troch, P. a., & Lyon, S. W. (2013). Separating physical and meteo-
 983 rological controls of variable transit times in zero-order catchments. *Water Re-*
 984 *sources Research*, *49*(11), 7644–7657. doi: 10.1002/2012WR013149
- 985 Hopp, L., Harman, C., Desilets, S., Graham, C., McDonnell, J., & Troch, P. (2009,
 986 jun). Hillslope hydrology under glass: confronting fundamental questions of
 987 soil-water-biota co-evolution at Biosphere 2. *Hydrology and Earth System*
 988 *Sciences Discussions*, *6*(3), 4411–4448. doi: 10.5194/hessd-6-4411-2009
- 989 Huxman, T., Troch, P., Chorover, J., Breshears, D. D., Saleska, S., Pelletier, J., ...
 990 Espeleta, J. (2009). The hills are alive: Earth science in a controlled environ-
 991 ment. *Eos*, *90*(14), 120. doi: 10.1029/2009EO140003
- 992 Jackson, C. R., Du, E., Klaus, J., Griffiths, N. A., Bitew, M., & McDonnell,
 993 J. J. (2016, aug). Interactions among hydraulic conductivity distribu-
 994 tions, subsurface topography, and transport thresholds revealed by a mul-
 995 titracer hillslope irrigation experiment. *Water Resources Research*. doi:
 996 10.1002/2015WR018364

- 997 Kaandorp, V. P., Louw, P. G. B. D., van der Velde, Y., & Broers, H. P. (2018).
 998 Transient groundwater travel time distributions and age-ranked storage-
 999 discharge relationships of three lowland catchments. *Water Resources Re-*
 1000 *search*, 48. doi: 10.1029/2017WR022461
- 1001 Kim, M. (2018). *Processes and Landscape Structure Underlying System Scale Hy-*
 1002 *drologic Transport: Theory, Experiment, and Modeling*. Doctoral Dissertation,
 1003 Johns Hopkins University.
- 1004 Kim, M., Pangle, L. A., Cardoso, C., Lora, M., Volkmann, T. H., Wang, Y., ...
 1005 Troch, P. A. (2016). Transit time distributions and StorAge Selection func-
 1006 tions in a sloping soil lysimeter with time-varying flow paths: Direct observa-
 1007 tion of internal and external transport variability. *Water Resources Research*,
 1008 52(9). doi: 10.1002/2016WR018620
- 1009 Kirkham, D. (1967). Explanation of paradoxes in Dupuit-Forchheimer Seep-
 1010 age Theory. *Water Resources Research*, 3(2), 609–622. doi: 10.1029/
 1011 WR003i002p00609
- 1012 Klemes, V. (1986). Dilettantism in Hydrology: Transition or Destiny? *Water Re-*
 1013 *sour. Res.*, 22(9), 177–188.
- 1014 Lawes, J. B., Gilbert, J. H., & Warington, R. (1882). On the amount and composi-
 1015 tion of the rain and drainage water collected at Rothamsted. *Journal of Royal*
 1016 *Agricultural Society of England*, 18, 1–71.
- 1017 Lyon, S. W., & Troch, P. A. (2007). Hillslope subsurface flow similarity: Real-
 1018 world tests of the hillslope Peclet number. *Water Resources Research*, 43(7),
 1019 1–9. doi: 10.1029/2006WR005323
- 1020 Małoszewski, P., & Zuber, a. (1982). Determining the turnover time of ground-
 1021 water systems with the aid of environmental tracers: 1. Models and their
 1022 applicability. *Journal of hydrology*, 57(3-4), 207–231. doi: 10.1016/
 1023 0022-1694(82)90147-0
- 1024 McDonnell, J. J., & Beven, K. (2014). Debates - The future of hydrological sciences:
 1025 A (common) path forward? A call to action aimed at understanding velocities,
 1026 celerities and residence time distributions of the headwater hydrograph. *Water*
 1027 *Resources Research*, 50, 5342–5350. doi: 10.1002/2013WR015141
- 1028 McDonnell, J. J., Brammer, D., Kendall, C., Hjerdt, N., Rowe, L., Stewart, M., &
 1029 Woods, R. (1998). Flow pathways on steep forested hillslopes: the tracer,

- 1030 tensiometer and trough approach. *Environmental Forest Science*, *54* (1997),
 1031 463–474.
- 1032 McDonnell, J. J., Sivapalan, M., Vaché, K., Dunn, S., Grant, G., Haggerty, R., ...
 1033 Weiler, M. (2007, jul). Moving beyond heterogeneity and process complex-
 1034 ity: A new vision for watershed hydrology. *Water Resources Research*, *43*(7),
 1035 n/a–n/a. doi: 10.1029/2006WR005467
- 1036 McGuire, K. J., & McDonnell, J. J. (2010). Hydrological connectivity of hillslopes
 1037 and streams: Characteristic time scales and nonlinearities. *Water Resources*
 1038 *Research*, *46*(10), 1–17. doi: 10.1029/2010WR009341
- 1039 Niemi, A. J. (1977). Residence time distributions of variable flow processes. *The In-*
 1040 *ternational Journal of Applied Radiation and Isotopes*, *28*, 855–860.
- 1041 Niu, G. Y., Pasetto, D., Scudeler, C., Paniconi, C., Putti, M., Troch, P. a., ... Zeng,
 1042 X. (2014). Incipient subsurface heterogeneity and its effect on overland flow
 1043 generation - Insight from a modeling study of the first experiment at the Bio-
 1044 sphere 2 Landscape Evolution Observatory. *Hydrology and Earth System*
 1045 *Sciences*, *18*(5), 1873–1883. doi: 10.5194/hess-18-1873-2014
- 1046 Norbiato, D., & Borga, M. (2008). Analysis of hysteretic behaviour of a hillslope-
 1047 storage kinematic wave model for subsurface flow. *Advances in Water Re-*
 1048 *sources*, *31*(1), 118–131. doi: 10.1016/j.advwatres.2007.07.001
- 1049 Nyberg, L. (1995). Water flow path interactions with soil hydraulic properties in till
 1050 soil at Gårdsjön, Sweden. *Journal of Hydrology*, *170*(1-4), 255–275. doi: 10
 1051 .1016/0022-1694(94)02667-Z
- 1052 Pangle, L. A., DeLong, S. B., Abramson, N., Adams, J., Barron-Gafford, G. A.,
 1053 Breshears, D. D., ... Zeng, X. (2015). The Landscape Evolution Observa-
 1054 tory: A large-scale controllable infrastructure to study coupled Earth-surface
 1055 processes. *Geomorphology*(August). doi: 10.1016/j.geomorph.2015.01.020
- 1056 Pangle, L. A., Kim, M., Cardoso, C., Lora, M., Meira Neto, A. A., Volkmann, T. H.,
 1057 ... Harman, C. J. (2017). The mechanistic basis for storage-dependent age dis-
 1058 tributions of water discharged from an experimental hillslope. *Water Resources*
 1059 *Research*, *53*, 2733–2754. doi: 10.1002/2016WR019901
- 1060 Pangle, L. A., Klaus, J., Berman, E. S. F., Gupta, M., & McDonnell, J. J. (2013). A
 1061 new multisource and high-frequency approach to measuring $\delta^2\text{H}$ and $\delta^{18}\text{O}$ in
 1062 hydrological field studies. *Water Resources Research*, *49*(11), 7797–7803. doi:

- 1063 10.1002/2013WR013743
- 1064 Rinaldo, A., Benettin, P., Harman, C. J., Hrachowitz, M., McGuire, K. J., Velde,
 1065 Y. V. D., . . . Botter, G. (2015). Storage selection functions: A coherent
 1066 framework for quantifying how catchments store and release water and solutes.
 1067 *Water Resources Research*, *51*, 1–8. doi: 10.1002/2015WR017273
- 1068 Rodriguez, N. B., McGuire, K. J., & Klaus, J. (2018). Time-Varying Storage – Wa-
 1069 ter Age Relationships in a Catchment with a Mediterranean Climate. *Water*
 1070 *Resources Research*, *0*(ja). doi: 10.1029/2017WR021964
- 1071 Sivapalan, M. (2003). Process complexity at hillslope scale, process simplicity at the
 1072 watershed scale: is there a connection? *Hydrological Processes*, *17*(5), 1037–
 1073 1041. doi: 10.1002/hyp.5109
- 1074 Sklash, M., Stewart, M., & Pearce, A. (1986). Storm Runoff Generation in Humid
 1075 Headwater Catchments: 2. A Case Study of Hillslope and Low-Order Stream
 1076 Response. *Water Resources Research*, *22*(8), 1273–1282.
- 1077 Torres, R., Dietrich, W. E., Montgomery, D. R., Anderson, S. P., & Loague, K.
 1078 (1998, aug). Unsaturated zone processes and the hydrologic response of a
 1079 steep, unchanneled catchment. *Water Resources Research*, *34*(8), 1865–1879.
 1080 doi: 10.1029/98WR01140
- 1081 Troch, P. A., Berne, A., Bogaart, P., Harman, C., Hilberts, A. G. J., Lyon, S. W.,
 1082 . . . Verhoest, N. E. C. (2013). The importance of hydraulic groundwa-
 1083 ter theory in catchment hydrology: The legacy of Wilfried Brutsaert and
 1084 Jean-Yves Parlange. *Water Resources Research*, *49*(9), 5099–5116. doi:
 1085 10.1002/wrcr.20407
- 1086 Troch, P. A., Paniconi, C., & Emiel van Loon, E. (2003). Hillslope-storage Boussi-
 1087 nesq model for subsurface flow and variable source areas along complex hill-
 1088 slopes: 1. Formulation and characteristic response. *Water Resources Research*,
 1089 *39*(11). doi: 10.1029/2002WR001728
- 1090 Troch, P. A., Van Loon, E., & Hilberts, A. (2002). Analytical solutions to a
 1091 hillslope-storage kinematic wave equation for subsurface flow. *Advances in*
 1092 *Water Resources*, *25*(6), 637–649. doi: 10.1016/S0309-1708(02)00017-9
- 1093 van den Heuvel, D., Troch, P., Booij, M., Niu, G., Volkmann, T., & Pangle, L.
 1094 (2018). Effects of differential hillslope-scale water retention characteristics on
 1095 rainfall-runoff response at the Landscape Evolution Observatory. *Hydrological*

- 1096 *Processes*(December 2017), 1–10. doi: 10.1002/hyp.13148
- 1097 van der Velde, Y., Heidbüchel, I., Lyon, S. W., Nyberg, L., Rodhe, A., Bishop, K.,
1098 & Troch, P. a. (2014). Consequences of mixing assumptions for time-variable
1099 travel time distributions. *Hydrological Processes*. doi: 10.1002/hyp.10372
- 1100 van der Velde, Y., Torfs, P. J. J. F., van der Zee, S. E. a. T. M., & Uijlenhoet, R.
1101 (2012, jun). Quantifying catchment-scale mixing and its effect on time-varying
1102 travel time distributions. *Water Resources Research*, *48*(6), W06536. doi:
1103 10.1029/2011WR011310
- 1104 van Genuchten, M. T. (1980). A Closed-form Equation for Predicting the Hydraulic
1105 Conductivity of Unsaturated Soils. *Soil Science Society of America Journal*,
1106 *44*(5), 892. doi: 10.2136/sssaj1980.03615995004400050002x
- 1107 Visser, A., Thaw, M., Deinhart, A., Bibby, R., Safeeq, M., Conklin, M., . . . Van der
1108 Velde, Y. (2019). Cosmogenic Isotopes Unravel the Hydrochronology and Wa-
1109 ter Storage Dynamics of the Southern Sierra Critical Zone. *Water Resources*
1110 *Research*. doi: 10.1029/2018WR023665
- 1111 Volkmann, T. H. M., Sengupta, A., Pangle, L. A., Dontsova, K., Barron-Gafford,
1112 G. A., Harman, C. J., . . . Troch, P. A. (2018). Controlled Experiments of
1113 Hillslope Coevolution at the Biosphere 2 Landscape Evolution Observatory:
1114 Toward Prediction of Coupled Hydrological, Biogeochemical, and Ecologi-
1115 cal Change. In J. Liu & W. Gu (Eds.), *Hydrology of artificial and controlled*
1116 *experiments* (chap. 2). London, UK: InTech. doi: 10.5772/intechopen.72325
- 1117 Wilusz, D. C., Harman, C. J., & Ball, W. P. (2017). Sensitivity of Catchment Tran-
1118 sit Times to Rainfall Variability Under Present and Future Climates. *Water*
1119 *Resources Research*, *53*(12), 10231–10256. doi: 10.1002/2017WR020894
- 1120 Wilusz, D. C., Harman, C. J., Ball, W. P., Maxwell, R. M., & Buda, A. R. (2020).
1121 Using Particle Tracking to Understand Flow Paths, Age Distributions, and
1122 the Paradoxical Origins of the Inverse Storage Effect in an Experimen-
1123 tal Catchment. *Water Resources Research*, *56*(4), e2019WR025140. doi:
1124 10.1029/2019WR025140
- 1125 Yang, J., Heidbüchel, I., Musolff, A., Reinstorf, F., & Fleckenstein, J. H. (2018).
1126 Exploring the Dynamics of Transit Times and Subsurface Mixing in a Small
1127 Agricultural Catchment. *Water Resources Research*, *54*(3), 2317–2335. doi:
1128 10.1002/2017WR021896